RICE UNIVERSITY

Overpressure and Earthquake Initiated Slope Failure in the Ursa Region, Northern Gulf of Mexico

by

Justin Lee Stigall

A THESIS SUBMITTED
IN PARTIAL FULFILLMENT OF THE
REQUIREMENTS FOR THE DEGREE

Master of Science

APPROVED, THESIS COMMITTEE:

Brandon Dugan, Assistant Professor
Earth Science

Julia K. Morgan, Professor
Earth Science

John B. Anderson, Professor
Earth Science

HOUSTON, TEXAS

AUGUST 2009

Abstract

Overpressure and Earthquake Initiated Slope Failure

in the Ursa Region, Northern Gulf of Mexico

By

Justin Lee Stigall

We use two-dimensional fluid flow and slope stability models to study the evolution of overpressure and slope stability in the Ursa region, northern Gulf of Mexico. Our model predictions match measured overpressures from Integrated Ocean Drilling Project Expedition 308 Site U1324 above 200 mbsf, but overpredicts deeper overpressures by 0.4-1.1 MPa. Slope stability models predict a slope failure at 61 ka on the eastern end of the Ursa region. This predicted failure corresponds to a mass transport deposit (MTD) that has been interpreted as a retrogressive failure initiated by high overpressure. Overpressure alone could not drive failure of a second MTD at ~27 ka. We predict that a magnitude 5 earthquake within 140 km of the Ursa region would initiate this failure. We conclude that overpressure could drive submarine slope failures and horizontal acceleration from earthquakes can further facilitate this process.

Acknowledgements

This research used samples and/or data provided by the Integrated Ocean Drilling Program (IODP). Funding for this research was provided by the Consortium for Ocean Leadership and Rice University. We thank Peter Flemings, Derek Sawyer, and Julia Schneider for providing valuable comments that strengthened this thesis.

Table of Contents

1. Introduction 1

2. Ursa region, Northern Gulf of Mexico 2

2.1 Sediment Source 4

2.2 Sediment Characterization 4

2.3 Stratigraphic Architecture 6

2.4 Mass Transport Deposits 8

2.5 Earthquake History 8

3. Overpressure Analysis 9

3.1 Sedimentation-Flow Model 9

3.2 Model Architecture 11

3.3 Overpressure at Sites U1324 and U1322 14

4. Slope Failure Analysis 17

4.1 Factor of Safety Model 17

4.2 Failures at Ursa 19

5. Pressure and Stability Summary 26

6. Conclusions 28

7. Notation 30

8. References 31

9. Appendix 36

1. Introduction

Slope failure is a common occurrence in shallow- and deep-water offshore environments. Slope failure initiation has been linked to zones of high pore pressure, wave loading and earthquakes [e.g., *Hampton et al.*, 1996; *Mello and Pratson*, 1999]. Slope failures are observed at the seafloor or preserved in the geologic record as displaced and disturbed sediment, known as mass transport deposits (MTDs) [*Hampton et al.*, 1996]. The origin, distribution, and timing of MTDs have been studied on the US continental shelf [*McAdoo et al.*, 2000], in Swiss lacustrine deposits [*Strasser et al.*, 2007], offshore Norway [*Kvalstad et al.*, 2005], and in many other locales worldwide.

When pore fluid cannot escape during sediment loading it will support a portion of the overburden; this generates overpressure (pressure in excess of hydrostatic) [*Gibson*, 1958; *Green and Wang*, 1986] which may decrease stability of a slope. Overpressure buildup slows the rate of increase of effective stress relative to the increase in overburden stress. In layered sedimentary systems with differential loading, overpressure can drive lateral flow through high permeability zones which can increase pore pressure in zones where significant overpressure may not have been created through one-dimensional loading [*Dugan and Flemings*, 2000; *Flemings et al.*, 2002; *Yardley and Swarbrick*, 2000].

Overpressured sediment has a lower shear strength, and therefore lower stability, than sediment in a hydrostatic system. Shear strength is the failure-resisting stress on the slope. Reduced shear strength will allow smaller driving stresses to initiate slope failure. The primary driving stresses (i.e., failure-initiating stresses) on a slope are created by gravitational and seismic loading [*Lambe and Whitman*, 1979; *Loseth*, 1998; *Mello and*

Pratson, 1999]. When driving stresses exceed shear strength, the slope is destabilized and it fails.

We use numerical models to constrain the evolution of overpressure and the mechanisms that cause slope failure on the low angle, low seismicity Ursa region of the northern Gulf of Mexico (GoM). Forward sedimentation models simulate the sediment loading, stress, pressure, and fluid flow history of the Ursa region. A factor of safety (FS) analysis of the resisting stresses to the shearing stresses from our sedimentation model is used to evaluate slope stability. Where overpressure alone is insufficient to initiate a failure. We determine the maximum distance from the Ursa region for a magnitude 5 earthquake required to induce failure. These models are used to constrain and understand the cause and timing of failures that created two MTDs in the Ursa region.

2. Ursa region, Northern Gulf of Mexico

The Ursa region of the Mississippi Canyon in the northern GoM is located approximately 200 km south-southeast of New Orleans, Louisiana, USA (Figure 1a). Difficulties in drilling for hydrocarbons through the poorly consolidated, overpressured sediment that encompasses much of this region resulted in detailed studies of the region [*Eaton*, 1999]. Studies of the Ursa region have explored sediment characteristics (e.g., permeability, consolidation), geomorphology, MTD character and development, fluid flow, and hydrocarbon potential [*Flemings et al.*, 2006; *Flemings et al.*, 2008; *Ostermeier et al.*, 2002; *Sawyer et al.*, 2007b; *Sawyer et al.*, in press].

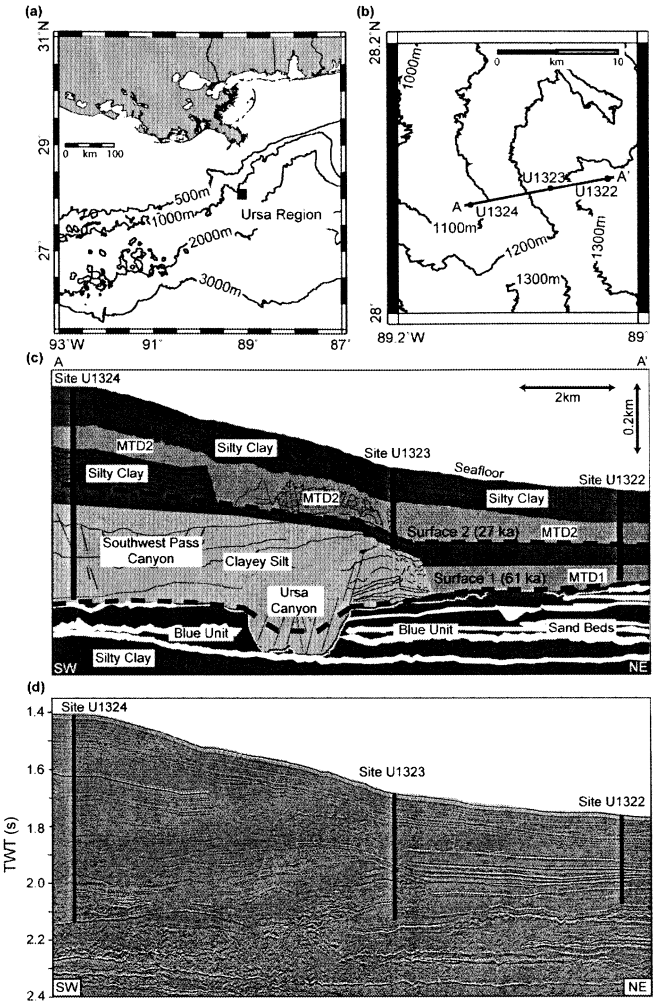

Figure 1. (a) Bathymetric map of the Northern Gulf of Mexico. (b) Bathymetry of the Ursa region with IODP Sites U1324, U1323, U1322 and cross-section A-A'. (c) Geological interpretation across the Ursa region (A-A') showing the IODP sites and general lithologic characterization [*Flemings et al.*, 2006; *Sawyer et al.*, 2007b]. (d) Seismic variable-density plot in two-way travel time. Blue unit is interbedded sand (white) and silty clay (dark grey), with overlying clayey silt (light grey) channel-levee deposits. All sediment above the clayey silt unit is silty clay. The region directly above the Blue unit at Site U1322 contains slope failures, labeled as mass transport deposit 1 (MTD1). The upper 100-200m of sediment contains mostly horizontal reflections until mass transport deposit 2 (MTD2), which extends across the entire region with slump blocks near Site U1323.

2.1 Sediment Source

Shallow sediments in the Ursa region are the result of multiple channel-levee systems deposited on a basin-floor fan [*Sawyer et al.*, 2007b]. The channel-levee systems formed the Ursa Canyon first (Figure 1c). The channel-levee system then migrated west of the Ursa Canyon through an avulsion event to form the Southwest Pass Canyon (Figure 1c)[*Sawyer et al.*, 2007b].

We suggest two potential sediment sources for the Ursa region over the last 65 ka: the Lagniappe Delta [*Fillon et al.*, 2004] and the Mississippi Delta [*Winker and Shipp*, 2002]. The Mobile and Pearl rivers formed the south-southwest facing lobate Lagniappe Delta on the shelf northeast of the Ursa region during the Late Wisconsinan glacial period [*Fillon et al.*, 2004; *Kindinger*, 1989]. At this time, the Mississippi river was discharging sediment west of the Ursa region off the coast of Louisiana [*Berryhill and Suter*, 1986; *Kindinger*, 1989]. During the rise and fall of sea level, the Lagniappe and Mississippi deltas delivered varied amounts of sediment to the slope, creating variable, rapid sedimentation (0.9 to > 30 mm/yr) with asymmetrical loading in the Ursa region (Figure 1c)[*Flemings et al.*, 2006].

2.2 Sediment Characterization

Integrated Ocean Drilling Program (IODP) Expedition 308 collected geotechnical and geophysical data to evaluate the magnitude and distribution of overpressure and the origin of slope instability in the Ursa region [*Flemings et al.*, 2006]. Cores were collected and analyzed from two sites in the Ursa region, Sites U1324 and U1322 (Figure 1b). The westernmost site, Site U1324, is located in 1057 m of water, and was drilled to 612

meters below seafloor (mbsf) (Figure 1c). Site U1322 is located on the eastern end of the region, approximately 12 km east of Site U1324 in 1330 m of water depth, and was drilled to 234.5 mbsf (Figure 1c).

Two main lithologies were identified at Sites U1324 and U1322 from core descriptions and grain size analyses: clayey silt and silty clay [*Flemings et al.*, 2006; *Sawyer et al.*, 2008]. The silty clay is composed of approximately 60% clay-sized particles and 40% silt-sized particles by mass. The clayey silt is composed of approximately 30% clay-sized particles and 70% silt-sized particles by mass [*Sawyer et al.*, 2008]. Site U1324 contains both lithologies. In general, silty clay exists from the seafloor to 365 mbsf and clayey silt extends from 365 to 612 mbsf. Site U1322 contains only silty clay. Immediately underlying the silty clay and clayey silt of Sites U1324 and U1322 is the Blue unit [*Flemings et al.*, 2006]. The Blue unit is an interbedded sand and silty clay package approximately 100 m thick (Figure 1c).

Geotechnical tests on silty clay and clayey silt samples show similar consolidation properties [*Long et al.*, 2008]. The porosity at IODP Sites U1324 and U1322 is approximately 80% at the seafloor and decreases to 38% by 120-140 mbsf. This reflects similar compression behavior of all sediments in the Ursa region. The main difference in geotechnical properties between these two lithologies is permeability. Permeability ranges from 10^{-17} to 10^{-20} m^2 for silty clay and from 10^{-16} to 10^{-18} m^2 for clayey silt [*Schneider et al.*, 2008].

Sedimentation rates in the Ursa region are based on planktonic foraminiferal biostratigraphy from Sites U1324 and U1322. Multiple age boundaries from 65 ka to 10 ka were identified and correlated between the two sites. The base of each site correlates

to 65 ka (top of the Blue unit), yielding an average sedimentation rate of 9.3 mm/yr for Site U1324 and 3.6 mm/yr for Site U1322. There is a large variation in sedimentation rate, from 0.86 mm/yr to over 30 mm/yr [*Flemings et al.*, 2006], which created an asymmetric loading of the Blue unit (Figure 1c).

2.3 Stratigraphic Architecture

The first major depositional event that shaped the shallow section (< 1 km) in the Ursa region was the deposition of the Blue unit. We assume the Blue unit overlies a homogeneous silty clay unit that was deposited before 70 ka and extends across the region (Figure 2a). The Blue unit formed as a basin-floor fan containing semi-continuous, stacked sand layers interbedded with silty clay [*Winker and Shipp*, 2002]. The deposition of the Blue unit ended at 65 ka (Figure 2b)[*Sawyer et al.*, 2007b].

Several channel-levee systems cut into the Blue unit, creating wide levee complexes before the channels were backfilled. We model two channel-levee systems. The Ursa Canyon channel-levee system created wide distal levee deposits of silty clay and clayey silt before being backfilled (Figure 2c). The Southwest Pass Canyon incised the Ursa Canyon levee and Blue unit from ~57-24 ka and created thicker levees of greater lateral extent than the Ursa Canyon (Figure 2d). Distal levee deposits (Figure 2e) and hemipelagic sediments covered the region with silty clay by 10 ka (Figure 2f)[*Flemings et al.*, 2006; *Sawyer et al.*, 2007b]. Low deposition (0.9 mm/yr) of silty clay from 10 ka to present yielded a modern-day seafloor slope of approximately 2°.

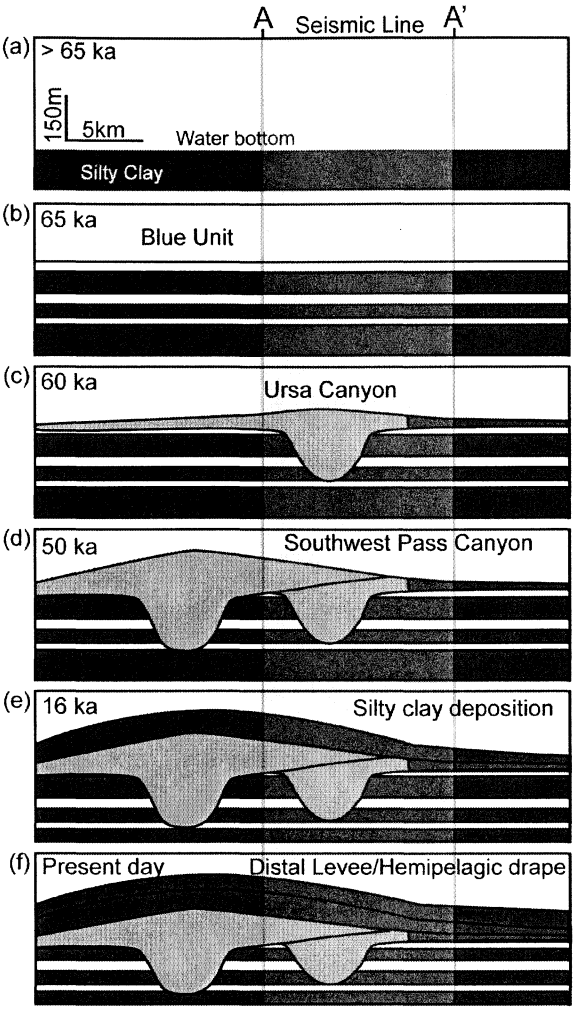

Figure 2. Simplified evolution of the Ursa region. Dark grey represents silty clay, light grey represents clayey silt, and white represents sand. Shaded section identifies region of cross-section A-A' (Figure 1c). (a) Before the deposition of the Blue unit, a base layer of silty clay was deposited under hydrostatic pressure. (b) The Blue unit was deposited leaving interbedded sand and silty clay by 65 ka. (c) The Ursa Canyon built levees of clayey silt with silty clay to the east by 60 ka. (d) By 50 ka the Southwest Pass Canyon and its levees formed. (e) Before 16 ka silty clay was differentially deposited across the region. (f) Distal levee/hemipelagic silty clay was deposited over the region by 10 ka, with little to no deposition (.9 mm/yr) until present day.

2.4 Mass Transport Deposits

Multiple MTDs have been interpreted from seismic data, core samples, and logging measurements in the Ursa region [*Dugan et al.*, 2007; *Sawyer et al.*, 2007b]. MTDs are identified from seismic data as chaotic, semi-transparent facies [*Posamentier*, 2004]. MTDs are also identified as higher density, more resistive zones on well logs and as folded or faulted sediment in cores [*Dugan et al.*, 2007; *Sawyer et al.*, 2007a]. The first MTD in the Ursa region, MTD1, is located in the eastern section of the region above the Blue unit and within the Ursa Canyon levee deposits (Figure 1c). MTD1 appears as a chaotic seismic facies; a result of multiple retrogressive slope failures which created a fluidized, long-run out failure [*Sawyer et al.*, in press]. A second MTD, MTD2, exists in the upper 100-200 m of the 12 km Ursa-region profile within the Southwest Pass Canyon levee deposits (Figure 1c) [*Sawyer et al.*, 2007b]. MTD2 contains a partially stratified seismic facies on its western end, which Sawyer *et al.* [in press] interpret is the result of a shorter run-out distance after failure.

2.5 Earthquake History

Seismicity studies in the GoM suggest that the region is seismically active despite the low number of recorded earthquakes. Seismicity has been attributed to subsidence related to sediment loading [*Frohlich*, 1982]; however, recent seismic activity has been linked to stick-slip displacement along growth or deep-crustal faults [*Angell and Hitchcock*, 2007], movement along salt-sediment interfaces [*Gangopadhyay and Sen*, 2008], and slope failure [*Nettles*, 2007]. Eight earthquakes (magnitude 3.2-5.9) recorded in the National Earthquake Information Center (NEIC) database for the northern GoM

from 1973-2009 occurred within 200 km of our study area. Earthquakes generate horizontal acceleration that, depending on the magnitude and distance from rupture to the slope, could contribute to slope failure.

3. Overpressure Analysis

A two-dimensional finite difference model, Basin2 [*Bethke et al.*, 1988], is used to simulate overpressure generation in the Ursa region. Sediment properties are derived from laboratory and shipboard measurements. Model geometry is defined by interpretation of seismic data (Figure 1c, Figure 2). Sedimentation rates are inferred from age data. We compare our predictions to pore pressure measurements from IODP Sites U1324 and U1322.

3.1 Sedimentation-Flow Model

The total vertical stress from overburden drives sediment consolidation when pore fluids can escape. When the rate of sediment loading exceeds the rate of fluid expulsion, the pore fluid pressure increases above hydrostatic [*Gibson*, 1958]. The rate of overpressure generation thus depends on sedimentation rate, sediment compressibility, and permeability.

To predict fluid pressure evolution, we simulate fluid flow by coupling Darcy's law, conservation of fluid mass, sediment loading, and pore fluid thermal expansion:

$$\phi\beta\frac{\partial P}{\partial t}=\frac{\partial}{\partial x}\left[\frac{k_x}{\mu}\left(\frac{\partial P}{\partial x}\right)\right]+\frac{\partial}{\partial z}\left[\frac{k_z}{\mu}\left(\frac{\partial P}{\partial z}-\rho g\right)\right]-\frac{1}{(1-\phi)}\frac{\partial\phi}{\partial t}+\phi\alpha\frac{\partial T}{\partial t}, \qquad (1)$$

where ϕ is porosity, β is fluid compressibility, P is pressure, t is time, k_x is horizontal permeability, k_z is vertical permeability, μ is dynamic viscosity, ϱ is pore fluid density, g is acceleration due to gravity, α is pore fluid thermal expansivity, and T is temperature [*Bethke et al.*, 1988].

Equation 1 depends on temperature, thus we simultaneously solve for conductive and advective heat flow:

$$\frac{\partial T}{\partial t} = \frac{\lambda}{\rho C_p}\nabla^2 T - u \cdot \nabla T, \tag{2}$$

where λ is thermal conductivity, C_p is specific heat capacity, and u is true fluid velocity [*Fowler*, 2005]. Thermal conductivity is assumed constant, 1.12 J/m·s·K, based on shipboard measurements on cores [*Flemings et al.*, 2006]. Basal heat flux is assumed to be 25 mW/m^2 [*Nagihara and Jones*, 2005]. Temperature does not play a significant role in overpressure generation in the shallow sediments of the Ursa region due to the small temperature range (4-18 °C).

Equation 1 also depends on porosity, which changes with effective stress. We model porosity change through a void ratio - vertical effective stress (e - $\sigma`_v$) model [*Long*, 2007]. Void ratio is directly related to porosity: $e = \phi/1\text{-}\phi$.

Void ratio change is modeled with a linear relationship between the compression index (C_c) and void ratio during consolidation [*Long*, 2007],

$$\frac{de}{d\log(\sigma`_v)} = C_c = A_c e + B_c. \tag{3}$$

Constants $A_c = 0.34$ and $B_c = 0.15$ were determined from a linear interpolation of compression data from silty clay from Site U1324 [*Long*, 2007; *Long et al.*, 2008]. During unloading (decreasing vertical effective stress), only the elastic portion of the

primary consolidation is recovered. We assume the unloading compressibility is 10% of the primary compressibility [*Corbet and Bethke*, 1992]. This yields $A_c = 0.034$ and $B_c = 0.015$ during unloading.

Additionally equation 1 and the fluid flow component of equation 2 require permeability constraints. We assume a log-linear relationship between porosity and permeability:

$$\log(k) = A_k \phi + B_k, \tag{4}$$

where A_k and B_k are empirical constants [*Mello et al.*, 1994]. A best-fit model to constant-rate-of-strain consolidation (CRSC) tests [*Long et al.*, 2008] yields $A_k = 9.0$ and $B_k = -22.16$ log m^2 for the vertical permeability of silty clay and $A_k = 9.2$ and $B_k = -19.77$ log m^2 for clayey silt [*Schneider et al.*, 2008]. The harmonic mean of permeability calculated during the CRSC tests is assumed to be the vertical permeability, and the arithmetic mean is assumed to be the horizontal permeability. This results in a permeability anisotropy (k_x/k_z) of 10 [*Schneider et al.*, 2008]. The permeability of sand within the Blue unit is set as isotropic and constant, 10^{-12} m^2 [*Freeze and Cherry*, 1979].

3.2 Model Architecture

We model a simplified stratigraphic architecture based on the seismic interpretation of the Ursa region (Figure 2). The distribution of each lithologic package is interpreted from seismic data and then each package is modeled as a separate depositional event (Figure 3a). This results in an Ursa region model with 14 deposition and 2 erosion events.

The lateral boundaries of our model are extended beyond the seismic section (Figure 1c) by 9 km west and 4 km east to eliminate boundary effects near the IODP Expedition 308 sites (Figure 3a). The model was expanded 5 km more to the west than to the east to include the entire Southwest Pass Canyon (Figure 2d). The model is bounded on the left, right and bottom by a no fluid-flow boundary. Basal heat flux is constant (25 mW/m^2), with no heat conduction through the western and eastern boundaries. The top of the model is a hydrostatic boundary at a constant temperature of 4°C.

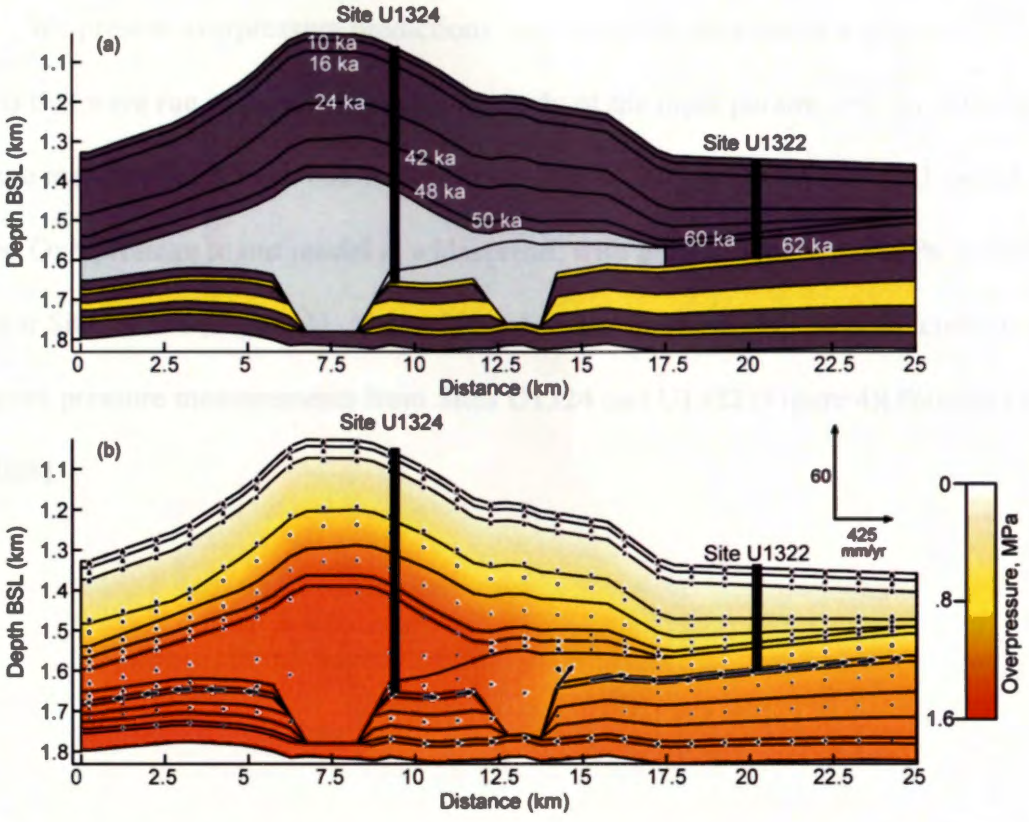

Figure 3. (a) 2D model at present day showing lithologic units and time horizons above the Blue unit sands. Dark grey represents silty clay, light grey represents clayey silt, and yellow represents sand. (b) Color contour plot of overpressure with stratigraphic lines (black, Figure 3a) and fluid velocity vectors. Present day overpressure reaches 1.5 MPa at Site U1324 and 1.1 MPa at Site U1322 (see also Figure 4). Fluid velocity vectors show the high permeability sand units in the Blue unit facilitated fluid flow from Site U1324 toward Site U1322.

3.3 Overpressure at Sites U1324 and U1322

We present overpressure predictions from the final iteration of a series of 2D models that were run as part of a sensitivity study of the input parameters. In situ pore pressure measurements from IODP Expedition 308 are compared with our 2D model results. Overpressure in our model is widespread, with a maximum of 1.5 MPa at present day near Site U1324 (Figure 3). Above 200 mbsf, our modeled pressures are consistent with pore pressure measurements from Sites U1324 and U1322 (Figure 4)[*Flemings et al.*, 2008].

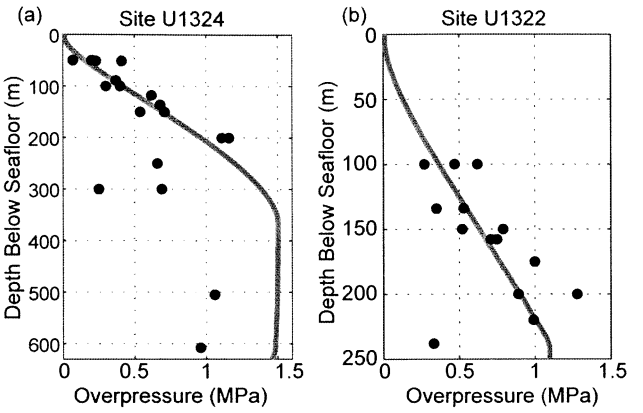

Figure 4. Overpressure model results (grey lines) and measurements (black circles) [*Flemings et al.*, 2008] at IODP Sites U1324 (a) and U1322 (b). Modeled overpressure at Site U1324 match observed measurements above 250 mbsf, but overpredict deeper overpressure. The modeled overpressure for Site U1322 matches measured overpressure except for the deepest observation.

From 200 to 300 mbsf at Site U1324, measured overpressure at Site U1324 decreases from 1.2 MPa to 0.6 MPa before increasing to ~1 MPa (Figure 4a). Predicted overpressure at Site U1324 below 200 mbsf is 0.3 MPa higher than the measured values, reaching a maximum overpressure of 1.5 MPa at 350 mbsf. Modeled overpressure at Site U1324 decreases slightly through the more permeable clayey silt from 350 mbsf to 612 mbsf (Figure 4a).

Measured overpressures at Site U1322 increase steadily with depth to 1 MPa at 225 mbsf until overpressure drops to ~0.3 MPa at 240 mbsf (Figure 4b)[*Flemings et al.*, 2008]. Our predicted overpressure at Site U1322 recreates the measured data above 225 mbsf. The measured overpressure near 240 mbsf at Site U1322 is 0.8 MPa lower than our model overpressure (Figure 4b). Repeated industry drilling through the Blue unit has facilitated pressure depletion from the Blue unit near the bottom of Site U1322 [*Flemings et al.*, 2008]. We do not model any drilling-related processes, which may account for our overprediction of pressure just above the Blue unit.

Our model simulates that high pore pressure near Site U1324 drives fluid primarily from west to east to the lower-pressured sediments near Site U1322 (Figure 3b). The higher permeability of the Blue unit has facilitated most of the lateral fluid flow within the Ursa region with true fluid velocity up to 250 mm/yr (Figure 3b). Higher deposition on the western end of the region during the filling of the Southwest Pass Canyon caused flow focusing from west to east. The lateral transfer of fluid pressure caused the Ursa region to have widespread overpressures, which has lowered the stability of the entire region. Without the high permeability Blue unit sands, lateral fluid flow would be impeded by the lower permeability clayey silt and silty clay.

4. Slope Failure Analysis

A slope stability model is used to evaluate the contribution of overpressure and horizontal earthquake acceleration to slope failure initiation in the Ursa region. Overpressure, total vertical stress, and hydrostatic vertical effective stress from our sedimentation-flow model are inputs for our slope failure model. We use an empirical model to estimate the horizontal earthquake acceleration for moderate earthquakes required to initiate failure in the Ursa region.

4.1 Factor of Safety Model

Slope stability is evaluated through an infinite slope analysis to predict the factor of safety (FS), the ratio of driving and resisting stresses on a slope:

$$FS = \frac{c + \left[\left(\sigma`_{vh} \cos^2\theta\right) - P^*\right]\tan\phi_f}{\sigma`_{vh} \cos\theta \sin\theta + F_{eq}}, \quad (5)$$

where c is sediment cohesion, P^* is overpressure, $\sigma`_{vh}$ is hydrostatic vertical effective stress, θ is seafloor slope angle, ϕ_f is internal friction angle, and F_{eq} is earthquake acceleration shear stress parallel to the slope [*Loseth*, 1998; *ten Brink et al.*, 2009]. Equation 5 assumes a homogenous, infinitely long slope with a failure surface parallel to the seafloor. We assume sediment cohesion, which is on the order of 1 kPa [*Day*, 1992], is negligible for the Ursa region where effective stresses and overpressures are 0.1-5 MPa. We use an internal friction angle equal to 26° based on triaxial strength experiments completed on sediments from Sites U1324 and U1322 [*Dugan and Germaine*, 2009]. The sedimentation-flow model provides hydrostatic effective stress and

overpressure inputs for equation 5. When FS > 1, the slope is considered stable. When FS ≤ 1, the slope is considered unstable.

Earthquakes can also contribute to destabilization of a slope. Shear stresses generated by earthquakes are assumed to result from the horizontal component of earthquake acceleration [*Hampton et al.*, 1996]. Assuming that horizontal acceleration from an earthquake is applied over a sufficiently long time period, we can model the seismically induced downslope shear stress as constant [*Hampton et al.*, 1996]. The horizontal earthquake acceleration term in equation 5, F_{eq}, is equal to $k_{crit} \cdot \sigma_v \cdot \cos^2\theta$, where k_{crit} is the critical horizontal earthquake acceleration required for FS = 1 and σ_v is total vertical stress. We solve equation 5 for k_{crit} where FS = 1 to find the critical horizontal earthquake acceleration needed to produce a failure [*ten Brink et al.*, 2009]:

$$k_{crit} = \frac{c + [(\sigma'_{vh}\cos^2\theta) - P^*]\tan\phi_f - \sigma'_{vh}\cos\theta\sin\theta}{\sigma_v \cos^2\theta}. \quad (6)$$

We then relate critical horizontal acceleration to peak spectral acceleration (k_{PSA}), which we model:

$$k_{PSA} = \frac{k_{crit}}{0.15 \cdot 3.5}, \quad (7)$$

where 0.15 relates horizontal acceleration (k_{crit}) to peak spectral acceleration as established for offshore California [*Lee et al.*, 2000] and 3.5 is an amplification factor for soft, slow velocity sediments such as those present in the Ursa region [*ten Brink et al.*, 2009].

We then input the required k_{PSA} for failure and an earthquake magnitude of 5, a reasonable upper bound for the GoM, into an empirical k_{PSA} model for earthquakes in North America [*Campbell*, 2003]:

$$\ln k_{PSA} = c_1 + f_1(M) + f_2(M,r) + f_3(r), \quad (8)$$

where M is earthquake magnitude, r is radius from rupture, c_1 is a constant and f is an empirically derived function. Equation 8 is then solved to determine the maximum distance to rupture that would produce a failure.

4.2 Failures at Ursa

We construct chronostability diagrams (Figures 5a,b) for two failure surfaces at Ursa (Figure 1c) to define FS through time. Surface 1 is immediately above the Blue unit and represents the base of MTD1; this surface is the 61 ka time horizon. Stability is also tracked along surface 2, representing the base of MTD2, the 27 ka time horizon.

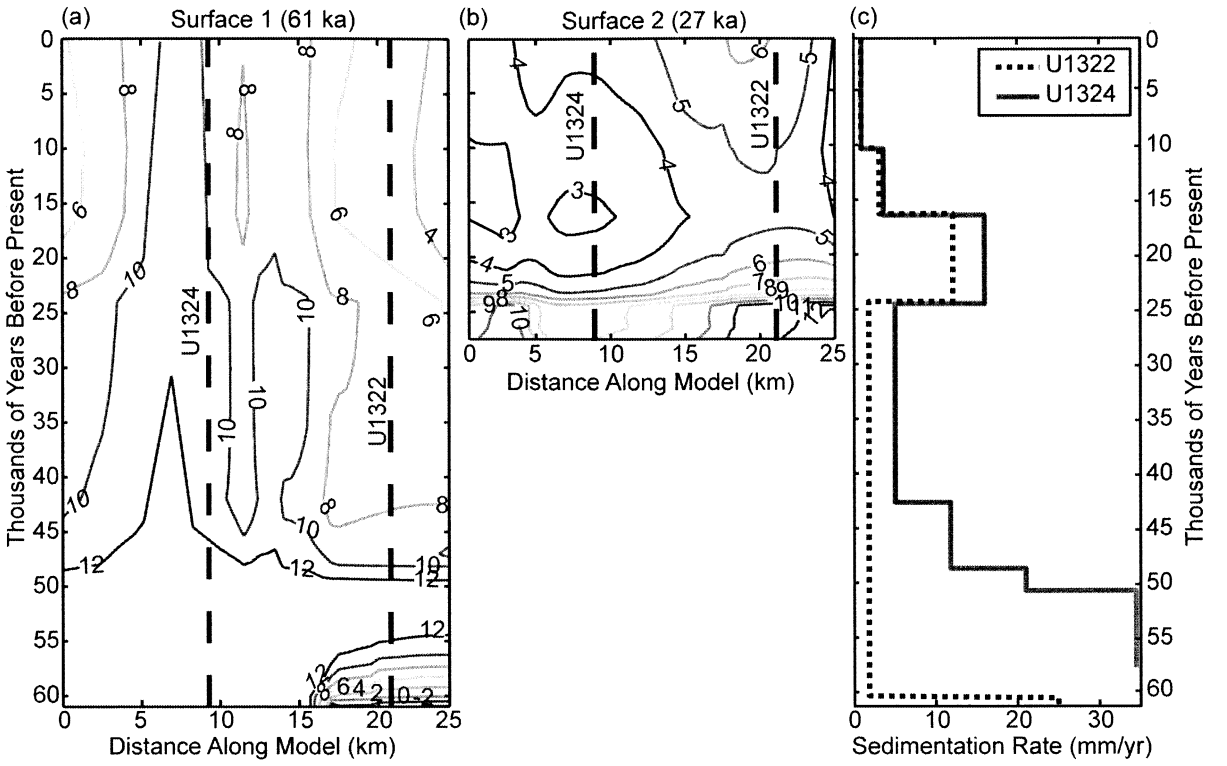

Figure 5. (a) Chronostability diagram with factor of safety contours for surface 1 (61 ka, located in Figure 1c). Dashed lines represent the locations of Sites U1324 and U1322. Surface 1 shows instability (FS < 1) on the eastern edge of our model (17–25 km) from 61-60 ka, corresponding with MTD1 (Figure 1c). (b) Chronostability diagram for surface 2 (27 ka, located in Figure 1c) below MTD2 (Figure 1c) does not show any instability. (c) Sedimentation rates used at Sites U1324 and U1322 used in our sedimentation-flow model. The lowest FS values correspond to periods of increased sedimentation near 62 ka and 25 ka.

The chronostability diagram for Surface 1 (Figure 5a) shows FS < 1 on the eastern side of the region (15-25 km) during the deposition of the Ursa Canyon levees from 62-60 ka. During this time silty clay was rapidly deposited (> 16 mm/yr) to the east of the Ursa canyon near Site U1322 (Figure 5c). Rapid sedimentation of low permeability silty clay created significant, shallow overpressure and low effective stress which destabilized the slope (FS < 1). After 60 ka, when the sedimentation rate decreased to 1.3 mm/yr at Site U1322 (Figure 5c), surface 1 has FS > 1. Surface 1 is stable (FS > 1) from 59 ka to present (Figure 5a).

The chronostability diagram for surface 2 (27 ka, Figure 5b) shows no periods with FS < 1. FS at surface 2 begins near 12 at 27 ka, and decreases rapidly at 25 ka, the start of a period of high sedimentation of silty clay at Sites U1324 and U1322 (Figure 5c). FS reaches a minimum of 3-5 across surface 2 near the end of rapid sedimentation (16 ka). FS at surface 2 then increases from 16 ka to present (Figure 5b). FS increases because shallow overpressure is able to dissipate to the seafloor when there is insufficient sedimentation to sustain overpressure generation. Thus, overpressure alone appears to be insufficient to create MTD2, suggesting an additional driving force is necessary for failure.

We calculate the required k_{PSA} to achieve failure (FS = 1) through time at surface 2 (Figure 6). We predict that k_{PSA} needs to be ≥ 0.002 at 27 ka. As the model evolves to present day, the required peak spectral acceleration required to initiate failure increases by an order of magnitude to $k_{PSA} = 0.02$ (Figure 6). The eastern and western ends of the model are the most susceptible to failure induced by horizontal earthquake acceleration

(low k_{PSA}) from 27 ka to present; the area near Site U1324 is the least susceptible (high k_{PSA})(Figure 6).

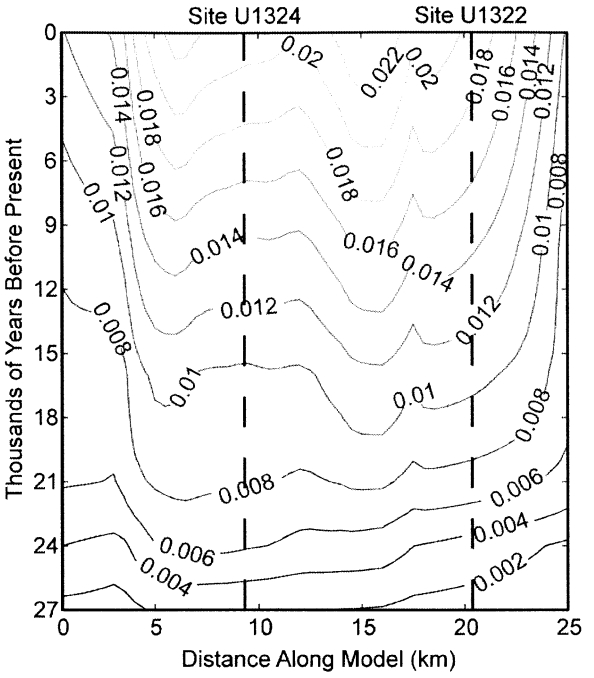

Figure 6. Contour plot of the peak spectral earthquake acceleration (k_{PSA}) necessary to achieve FS = 1 at surface 2 (located in Figure 1c) from 27 ka to present. Dashed lines represent the locations of Sites U1324 and U1322. At 27 ka, when surface 2 was deposited, the k_{PSA} required for failure was 0.002. At present day, k_{PSA} required to drive instability on surface 2 is an order of magnitude higher, $k_{PSA} = 0.02$.

We predict a maximum distance to rupture from the Ursa region that would produce the k_{PSA} required to produce failure. At 27 ka, a magnitude 5 earthquake 140 km from the Ursa region would have destabilized surface 2 (Figure 7). At present day, the same magnitude earthquake would need to be within 20 km of the Ursa region to destabilize surface 2 (Figure 7). A lower magnitude earthquake (<5) could also initiate failure, but it would need to be closer to the Ursa region than the predicted radius for a magnitude 5 earthquake. Data from 1973-2009 show that earthquakes in the Ursa region are within the magnitude-radius range capable of driving failure for surface 2 at 27 ka (Figure 7). Assuming that earthquakes in the past 27 ka for the Ursa region are similar in size and distribution, we interpret that an earthquake initiated the slope failure that created MTD2.

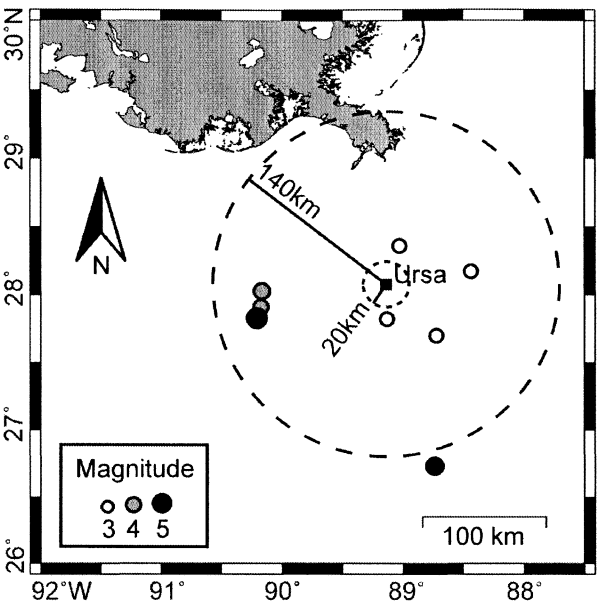

Figure 7. Earthquake-stability map of the Ursa region based on the 27 ka surface below MTD2 (surface 2, located in Figure 1c). Dashed circles represent the distance to rupture required for a magnitude 5 earthquake to destabilize surface 2 at 27 ka (140 km) and present day (20 km). Seismicity from 1973-2009 (solid circles) are magnitude 3.6 to 5.9 earthquakes from the National Earthquake Information Center (NEIC) database.

5. Pressure and Stability Summary

The primary cause of high overpressure in the Ursa region is high sedimentation rates; > 30 mm/yr at the start of the deposition of the channel-levee systems at 62 ka, and > 16 mm/yr during the deposition of the Southwest Pass Canyon at 25 ka. Rapid loading near Site U1324 drove fluids east toward Site U1322 which increased the pressure in the east. During periods of low sedimentation overpressure dissipates, but only slightly due to the low permeability of the Ursa sediments. Even though the Ursa region had very little sedimentation from 10 ka to present, it retains high overpressure in shallow sediments. Figures A1-A14 in the appendix show how overpressure, true fluid velocity, and factor of safety changed from 65 ka to present.

Above 200 mbsf our model accurately reproduces present day overpressure at Sites U1324 and U1322. However, our model did not reproduce the abrupt decrease in overpressure below 200 mbsf at Site U1324 and below 225 mbsf at Site U1322. In order to model this phenomenon we need a mechanism for overpressure dissipation from the clayey silt at Site U1324. The permeability of this unit does not allow pressure to drain within 65 ka. Increasing permeability anisotropy (e.g. $k_x/k_z > 10$) within the clayey silt would increase lateral fluid flow. Increased lateral flow would allow overpressure below 200 mbsf at Site U1324 to dissipate more quickly without decreasing the overpressure of the overlying silty clay.

Site U1322 also has an abrupt decrease in overpressure that is inconsistent with our model predictions. One measurement, near the Blue unit at 240 mbsf, is 0.8 MPa lower than our model prediction. *Flemings et al.* [2008] propose that the overpressure decrease at the base of Site U1322 could have been caused by industry drilling through

the Blue unit. This may have facilitated overpressure drainage near the Blue unit. We have not modeled drilling-induced conditions, thus we do not address this phenomenon at Site U1322.

With FS ≤ 1, surface 1 could have failed at any time from 61-60 ka (see Appendix and Figure 5). The timing and extent of this zone of low FS coincides with MTD1, where failure occurred only east of the Ursa canyon within the silty clay levee deposits. While we only show results for surface 1 in this region, our model predicts FS < 1 for multiple surfaces within the silty clay deposited during this time period. The seismic interpretation shows that MTD1 extends vertically from the top of the Blue unit to the top of the Ursa Canyon levee deposits. *Sawyer et al.* [in press] suggest that MTD1 is composed of sediment that retrogressively failed after an initial failure due to continuous, high overpressure. Consistent with this idea, our model demonstrates that rapid loading from 61-60 kya created a continuous source of overpressure that drove failure at the eastern end of the Ursa region near Site U1322. This initial failure then evolved into a long-run-out failure that created MTD1.

From 27 ka to 10 ka, when the failure that created MTD2 occurred, overpressure alone could not drive FS ≤ 1. Increasing the sedimentation rate during this period would increase overpressure and decrease FS, however this would create unreasonably high overpressure in the modern environment. Thus we interpret an alternate source contributed to slope failure.

Sediment weakened by high overpressure in the Ursa region could have failed during an earthquake. The pattern of earthquake occurrence in the northern GoM coupled with the low FS due to high, shallow overpressure at the base of MTD2, suggests that the

failure that caused MTD2 was initiated by the combination of causes. By combining overpressure models with earthquake acceleration models we characterize a mechanism for the slope failure that created MTD2: moderate overpressure from rapid sedimentation coupled with horizontal earthquake acceleration of a magnitude 5 earthquake within 140 km of the Ursa region.

6. Conclusions

The generation of overpressure is a critical factor in the stability of the low angle slope of the Ursa region. We predict overpressure at Site U1324 consistent with measured overpressures above 200 mbsf. Below 200 mbsf at Site U1324 our model overpredicts measured overpressure by 0.4-1.1 MPa. Our model matches measured overpressures at Site U1322 for all but the deepest measurement. Lateral fluid flow through the permeable Blue unit is critical to controlling the regional pressure field. Flow from west to east in the Ursa region has lowered overpressure at Site U1324 and increased overpressure at Site U1322 creating the pressure field observed today. This increase in overpressure at Site U1322 is critical to the stability of the eastern side of the Ursa region.

We show that factor of safety analysis can predict overpressure- and earthquake-induced slope failures in the Ursa region. The conditions that initiated a slope failure are simulated, creating MTD1 on the eastern end of the Ursa region at 61 ka. Sustained, high overpressure is believed to be the trigger for this massive, long-run-out, retrogressive failure. Failure that created MTD2 was facilitated by high overpressure, but horizontal acceleration resulting from a magnitude 5 earthquake within 140 km of Ursa was required to destabilize the slope. Earthquakes of magnitude 5 have occurred within this

maximum rupture distance. An earthquake of magnitude < 5 could also initiate a failure, but it would need to originate closer to the Ursa region. We therefore propose that in some cases overpressure drives failure on low angle slopes, however earthquakes, even on passive margins, may play a critical role in initiating slope failure in sediments weakened by overpressure.

7. Notation

A_c coefficient for C_c model, dimensionless.
A_k coefficient for k model, log[m^2].
B_c coefficient for C_c model, dimensionless.
B_k coefficient for k model, log[m^2].
c cohesion, MPa.
C_c compression index, dimensionless.
C_p specific heat capacity, J/kg·K.
e void ratio, dimensionless.
g acceleration due to gravity, m/s^2.
k permeability, m^2.
k_{crit} critical horizontal earthquake acceleration, dimensionless.
k_{PSA} peak spectral earthquake acceleration, dimensionless.
k_x horizontal permeability, m^2.
k_z vertical permeability, m^2.
M earthquake moment magnitude, dimensionless.
P pressure, MPa.
P* overpressure, MPa.
r radius from earthquake rupture, km.
t time, s.
T temperature, K.
u true fluid velocity, m/s.
α pore fluid thermal expansivity, 1/K.
β fluid compressibility, 1/MPa.
θ slope angle, degrees.
λ thermal conductivity, J/m·s·K.
μ dynamic viscosity, MPa·s.
ρ fluid density, kg/m^3.
$\sigma`_v$ vertical effective stress, MPa.
$\sigma`_{vh}$ hydrostatic vertical effective stress, MPa.
ϕ porosity, dimensionless.
ϕ_f internal friction angle, degrees.

8. References

Angell, M., and C. Hitchcock (2007), A Geohazard Perspective of Recent Seismic Activity in the Northern Gulf of Mexico. OTC Paper #19035, in *Offshore Technology Conference*, edited, Houston, TX.

Berryhill, H. L., Jr., and J. R. Suter (1986), Late Quaternary Facies and Structure, Northern Gulf of Mexico: Interpretations from Seismic Data, *AAPG Studies in Geology*, *23*, 131-189.

Bethke, C. M., W. J. Harrison, C. Upson, and S. P. Altaner (1988), Supercomputer analysis of sedimentary basins, *Science*, *239*(4837), 261-267.

Campbell, K. W. (2003), Prediction of Strong Ground Motion Using the Hybrid Empirical Method and Its Use in the Development of Ground-Motion (Attenuation) Relations in Eastern North America, *Bulletin of the Seismological Society of America*, *93*(3), 1012-1033, doi:10.1785/0120020002.

Corbet, T. F., and C. M. Bethke (1992), Disequilibrium fluid pressures and groundwater flow in the Western Canada sedimentary basin, *Journal of Geophysical Research*, *97*(B5), 7203-7217.

Day, R. W. (1992), Effective Cohesion for Compacted Clay, *Journal of Geotechnical Engineering*, *118*(4), 611-619.

Dugan, B., and P. B. Flemings (2000), Overpressure and fluid flow in the New Jersey continental slope: Implications for slope failure and cold seeps, *Science*, *289*(5477), 288-291, doi:10.1126/science.289.5477.288.

Dugan, B., and J. T. Germaine (2009), Data report: strength characteristics of sediments from IODP Expedition 308, Sites U1322 and U1324. In Flemings, P.B., Behrmann, J.H., John, C.M., and the Expedition 308 Scientists, Proc. IODP, 308: College Station, TX (Integrated Ocean Drilling Program Management International, Inc.), doi:10.2204/iodp.proc.308.210.2009.

Dugan, B., P. B. Flemings, D. E. Sawyer, G. J. Iturrino, J. C. Moore, and J. Schneider (2007), Physical properties of mass transport complexes in the Ursa Region, Northern Gulf of Mexico (IODP Expedition 308) Determined from log, core and seismic data. OTC Paper #18704, in *Offshore Technology Conference*, edited, Houston, TX.

Eaton, L. F. (1999), Drilling Through Deepwater Shallow Water Flow Zones at Ursa, in *SPE/IADC Drilling Conference*, edited, Amsterdam, Netherlands.

Fillon, R. H., B. Kohl, and H. H. Roberts (2004), Late quaternary deposition and paleobathymetry at the shelf-slope transition, ancestral mobile river delta complex, northeaster Gulf of Mexico, in *Late Quaternary Stratigraphic Evolution of the Northern Gulf of Mexico Margin*, edited, Society for Sedimentary Geology Special Publication.

Flemings, P. B., B. B. Stump, T. Finkbeiner, and M. Zoback (2002), Flow focusing in overpressured sandstones: Theory, observations, and applications, *American Journal of Science*, *302*(10), 827-855, doi:10.2475/ajs.302.10.827.

Flemings, P. B., J. H. Behrmann, C. M. John, and Expedition 308 Scientists (2006), Proc. IODP, 308: College Station, TX (Integrated Ocean Drilling Program Management International, Inc.), doi:10.2204/iodp.proc.308.101.2006.

Flemings, P. B., H. Long, B. Dugan, J. Germaine, C. M. John, J. H. Behrmann, D. Sawyer, and Expedition 308 Scientists (2008), Pore pressure penetrometers document high overpressure near the seafloor where multiple submarine landslides have occurred on the continental slope, offshore Louisiana, Gulf of Mexico (vol 269, pg 309, 2008), *Earth and Planetary Science Letters*, *274*(1-2), 269-283, doi:10.1016/J.Epsl.2008.06.027.

Fowler, C. M. R. (2005), *The Solid Earth*, 2nd ed., Cambridge University Press, Cambridge.

Freeze, R. A., and J. A. Cherry (1979), *Groundwater*, Prentice-Hall, Englewood Cliffs, NJ.

Frohlich, C. (1982), Seismicity of the Central Gulf of Mexico, *Geology*, *10*(2), 103-106.

Gangopadhyay, A., and M. K. Sen (2008), A possible mechanism for the spatial distribution of seismicity in northern Gulf of Mexico, *Geophysical Journal International*, *175*(3), 1141-1153.

Gibson, R. E. (1958), The progress of consolidation in a clay layer increasing in thickness with time, *Geotechnique*, *8*, 171-182.

Green, D. H., and H. F. Wang (1986), Fluid pressure response to undrained compression in saturated sedimentary rock, *Geophysics*, *51*(4), 948-956.

Hampton, M. A., H. J. Lee, and J. Locat (1996), Submarine Landslides, *Rev. Geophys.*, *34*(1), 33-59.

Kindinger, J. L. (1989), Depositional History of the Lagniappe Delta, Northern Gulf of Mexico, *Geo-Marine Letters*(9), 59-66.

Kvalstad, T. J., L. Andresen, C. F. Forsberg, K. Berg, P. Bryn, and M. Wangen (2005), The Storegga slide: evaluation of triggering sources and slide mechanics, *Marine and Petroleum Geology*, *22*(1-2), 245-256.

Lambe, T. W., and R. V. Whitman (1979), *Soil Mechanics, SI Version*, John Wiley & Sons, New York.

Lee, H. J., J. Locat, P. Dartnell, D. Minasian, and F. Wong (2000), A GIS-based regional analysis of the potential for shallow-seated submarine slope failure, paper presented at Eighth International Symposium on Landslides, Cardiff, Wales, June, 2000.

Long, H. (2007), Interpreting Pore Pressure in Marine Mudstones with Pore Pressure Penetrometers, in Situ Data, and Laboratory Measurements, Ph.D. thesis, Pennsylvania State University, University Park, PA, USA.

Long, H., P. B. Flemings, J. T. Germaine, D. M. Saffer, and B. Dugan (2008), Data report: consolidation characteristics of sediments from IODP expedition 308, Ursa Basin, Gulf of Mexico, *In Flemings PB, John C, (Eds.), Proc. IODP, Scientific Results, Expedition 308.*

Loseth, T. M. (1998), *Submarine Massflow Sedimentation: Computer Modeling and Basin-Fill Stratigraphy*, Springer-Verlag, New York.

McAdoo, B. G., L. F. Pratson, and D. L. Orange (2000), Submarine landslide geomorphology, U.S. continental slope., *Marine Geology*, *169*, 103-136.

Mello, U. T., and L. F. Pratson (1999), Regional slope stability and slope-failure mechanics from the two-dimensional state of stress in an infinite slope, *Marine Geology*, *154*, 339-356.

Mello, U. T., G. D. Karner, and R. N. Anderson (1994), A physical explanation for the positioning of the depth to the top of overpressure in shale dominated sequences in the Gulf Coast basin, *Journal of Geophysical Research*, *99*, 2775-2789.

Nagihara, S., and K. O. Jones (2005), Geothermal heat flow in the northeast margin of the Gulf of Mexico, *Aapg Bulletin*, *89*(6), 821-831, doi:10.1306/01170504057.

Nettles, M. (2007), Analysis of the February 10, 2006, Gulf of Mexico earthquake from global and regional seismic data. OTC Paper #19099, in *Offshore Technology Conference*, edited, Houston, TX.

Ostermeier, R. M., J. H. Pelletier, C. D. Winker, J. W. Nicholson, F. H. Rambow, and K. M. Cowan (2002), Dealing with shallow-water flow in the deepwater Gulf of Mexico, *The Leading Edge*, *21*(7), 660-668, doi:10.1190/1.1497320.

Posamentier, H. W. (2004), Stratigraphy and geomorphology of deep-water mass transport complexes based on 3D seismic data OTC Paper #16740, in *Offshore Technology Conference*, edited, Houston, TX.

Sawyer, D. E., P. B. Flemings, B. Dugan, and Expedition Scientists (2007a), Lateral variations in core, log, and seismic attributes of a mass transport complex in the Ursa Region, IODP Expedition 308, Northern Gulf of Mexico. OTC Paper #19098, in *Offshore Technology Conference*, edited, Houston, TX.

Sawyer, D. E., P. B. Flemings, R. C. Shipp, and C. D. Winker (2007b), Seismic geomorphology, lithology, and evolution of the late Pleistocene Mars-Ursa turbidite region, Mississippi Canyon area, northern Gulf of Mexico, *AAPG Bulletin*, *91*(2), 215-234, doi:10.1306/08290605190.

Sawyer, D. E., R. Jacoby, P. B. Fleming, and J. T. Germaine (2008), Data report: particle size analysis of sediments in the Ursa Basin, IODP Expedition 308 Sites U1324 and U1322, northern Gulf of Mexico. In Flemings, P.B., Behrmann, J.H., John, C.M., and the Expedition 308 Scientists, Proc. IODP, 308: College Station, TX (Integrated Ocean Drilling Program Management International, Inc.).

Sawyer, D. E., P. B. Fleming, B. Dugan, and J. T. Germaine (in press), Retrogressive Failures Recorded in Mass Transport Deposits in the Ursa Basin, Northern Gulf of Mexico, *Journal of Geophysical Research.*

Schneider, J., P. B. Flemings, B. Dugan, H. Long, J. T. Germaine, and D. M. Saffer (2008), Porosity vs. permeability behavior of shallow mudstones in the Ursa Basin, deepwater Gulf of Mexico, *Eos Trans. AGU, 89(53), Fall Meet. Suppl., Abstract OS11A-1105*.

Strasser, M., S. Stegmann, F. Bussmann, F. S. Anselmetti, B. Rick, and A. Kopf (2007), Quantifying subaqueous slope stability during seismic shaking: Lake Lucerne as model for ocean margins, *Marine Geology*, *240*(1-4), 77-97.

ten Brink, U. S., H. J. Lee, E. L. Geist, and D. Twichell (2009), Assessment of tsunami hazard to the U.S. East Coast using relationships between submarine landslides and earthquakes, *Marine Geology*, *264*(1-2), 65-73.

Winker, C. D., and R. C. Shipp (2002), Sequence stratigraphic framework for prediction of shallow water flow in the greater Mars-Ursa Area, Mississippi Canyon Area, Gulf of Mexico continental slope (abs.) in J. Armentrout, ed., Sequence stratigraphic models for exploration and production: evolving methodology, emerging models, and application histories, paper presented at SEPM Gulf Coast Section 22nd Annual Research Conference.

Yardley, G. S., and R. E. Swarbrick (2000), Lateral transfer: a source of additional overpressure?, *Marine and Petroleum Geology*, *17*(4), 523-537.

9. Appendix

Figures A1-A14 show a time series of our final model from 65 ka to present in 5 ka time steps. The top diagram of each figure is a color contour plot of overpressure in MPa with stratigraphy (black lines) and true fluid velocities (arrows) in mm/yr. The bottom diagram of each figure is a color contour plot of factor of safety with stratigraphy. Time stamp at bottom indicates the time period represented in the figure.

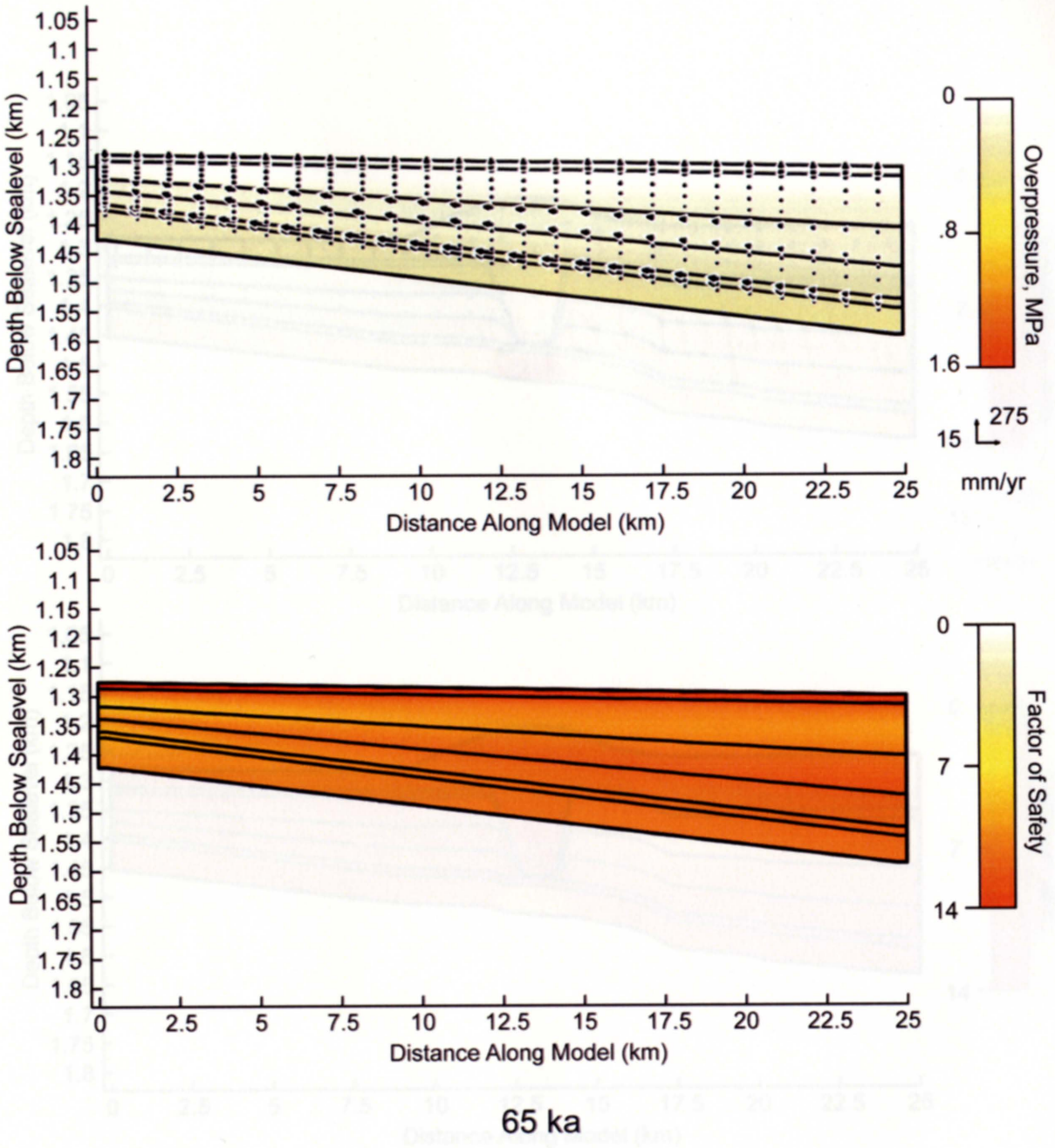
Depth Below Sealevel (km)
1.05
1.1
1.15
1.2
1.25
1.3
1.35
1.4
1.45
1.5
1.55
1.6
1.65
1.7
1.75
1.8
0
2.5
5
7.5
10
12.5
15
17.5
20
22.5
25
Distance Along Model (km)
0
.8
1.6
Overpressure, MPa
275
15
mm/yr
Depth Below Sealevel (km)
Distance Along Model (km)
0
7
14
Factor of Safety
65 ka

Figure A1.

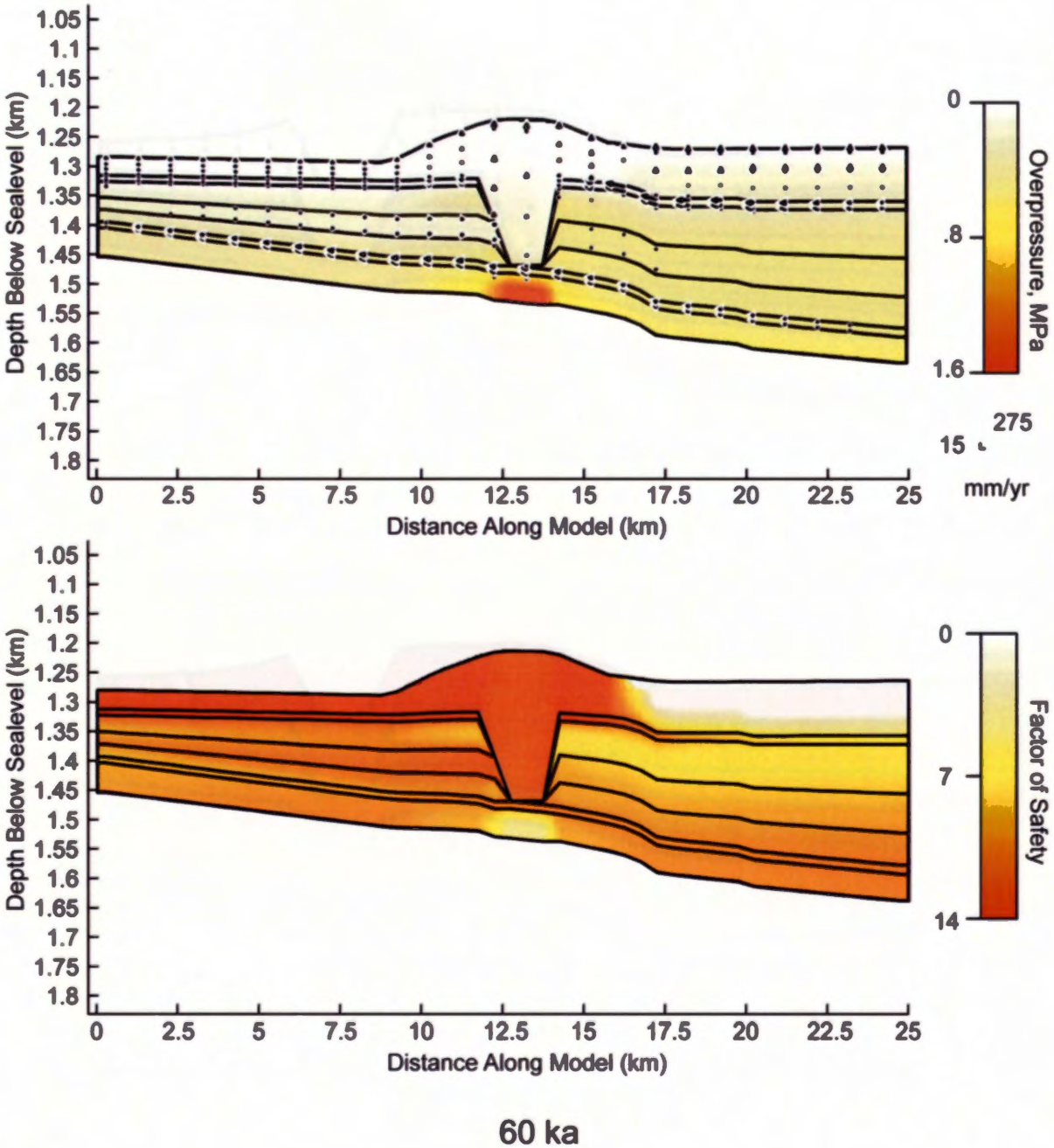
Depth Below Sealevel (km)
1.05
1.1
1.15
1.2
1.25
1.3
1.35
1.4
1.45
1.5
1.55
1.6
1.65
1.7
1.75
1.8
0
2.5
5
7.5
10
12.5
15
17.5
20
22.5
25
Distance Along Model (km)
0
.8
1.6
Overpressure, MPa
275
15
mm/yr
Depth Below Sealevel (km)
Distance Along Model (km)
0
7
14
Factor of Safety
60 ka

Figure A2.

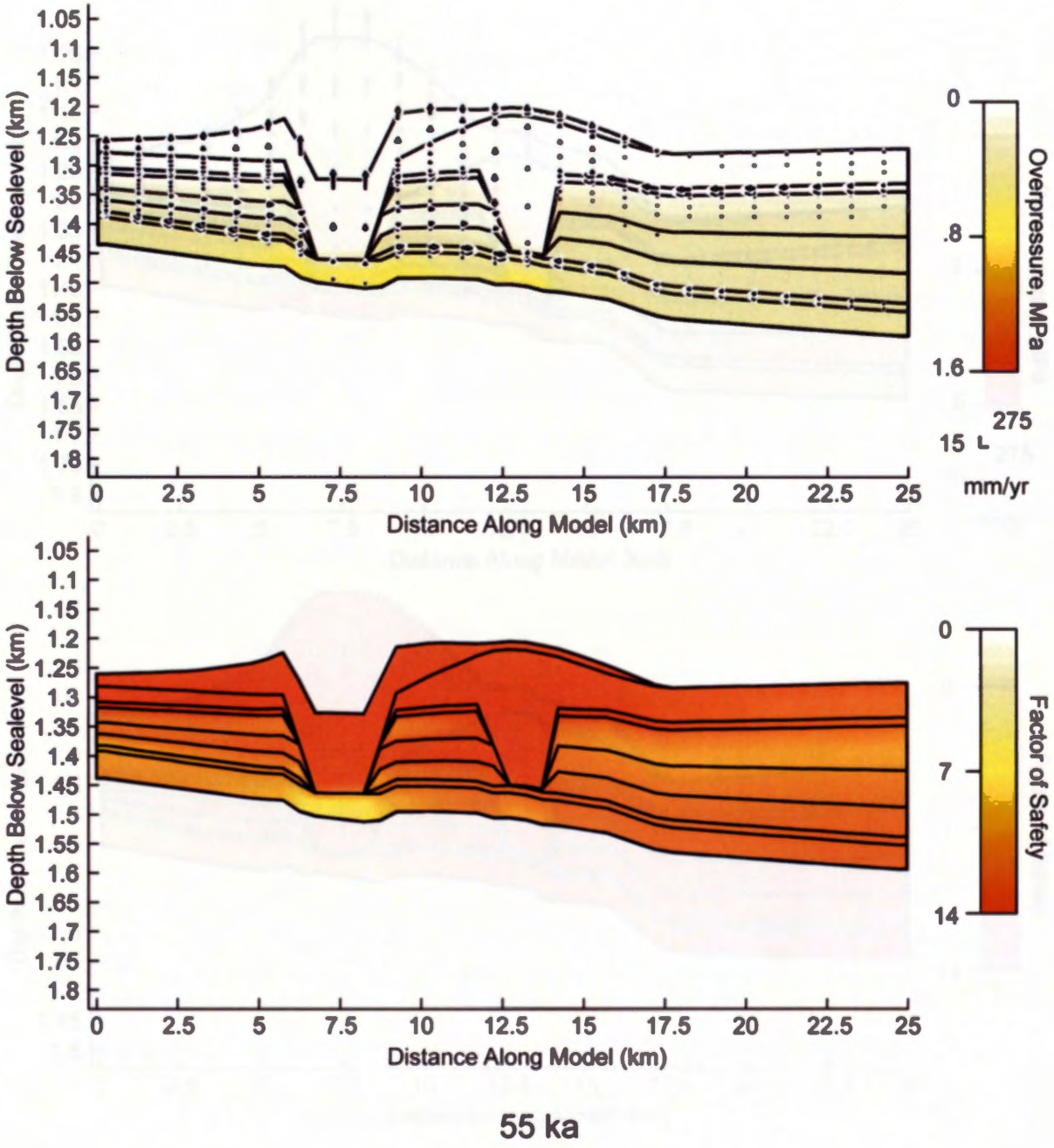
Depth Below Sealevel (km)
1.05
1.1
1.15
1.2
1.25
1.3
1.35
1.4
1.45
1.5
1.55
1.6
1.65
1.7
1.75
1.8
0
2.5
5
7.5
10
12.5
15
17.5
20
22.5
25
Distance Along Model (km)
0
.8
1.6
Overpressure, MPa
15
275
mm/yr
Depth Below Sealevel (km)
Distance Along Model (km)
0
7
14
Factor of Safety
55 ka

Figure A3.

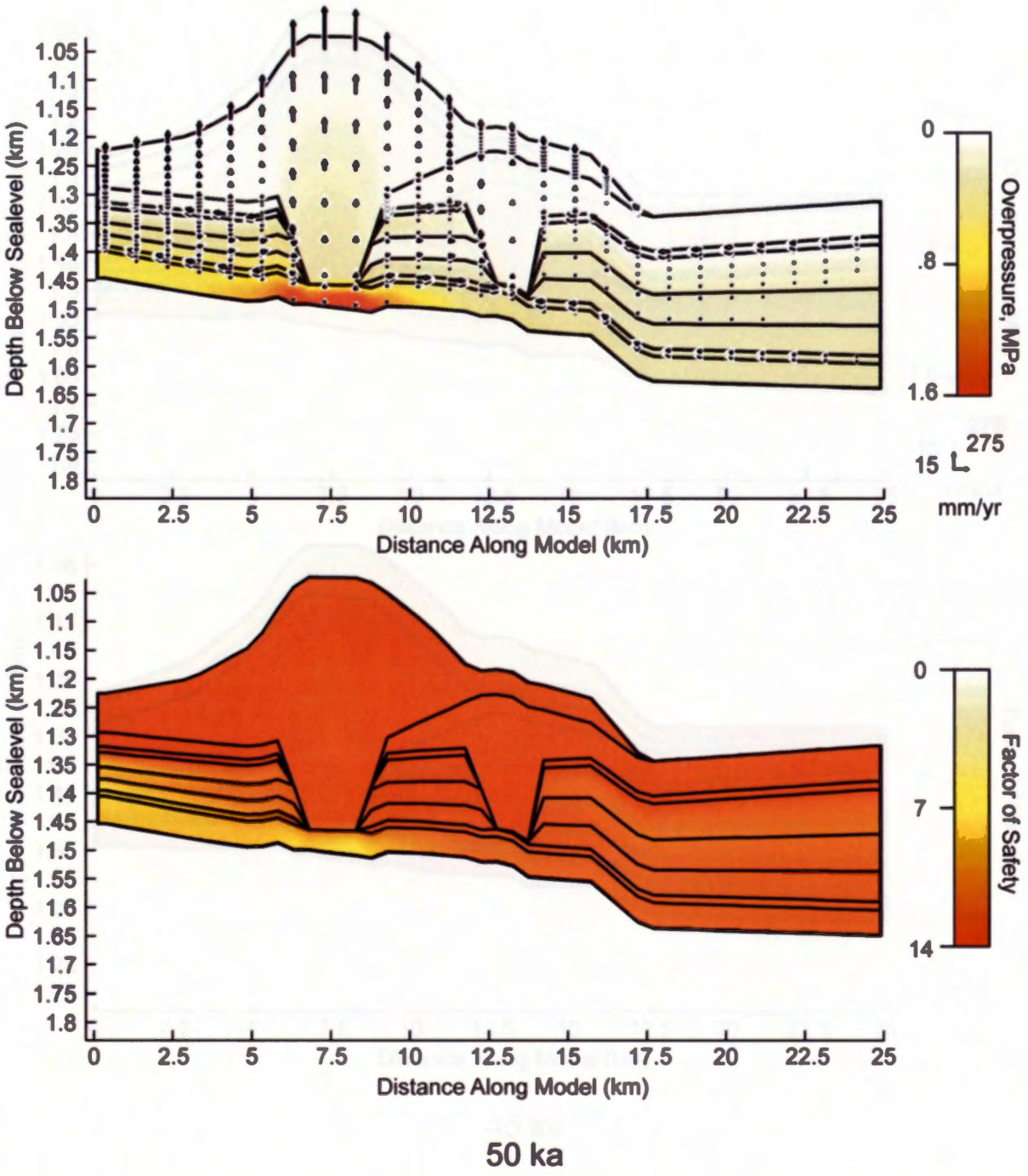
Depth Below Sealevel (km)
1.05
1.1
1.15
1.2
1.25
1.3
1.35
1.4
1.45
1.5
1.55
1.6
1.65
1.7
1.75
1.8
0
2.5
5
7.5
10
12.5
15
17.5
20
22.5
25
Distance Along Model (km)
0
.8
1.6
Overpressure, MPa
15
275
mm/yr
Depth Below Sealevel (km)
Distance Along Model (km)
0
7
14
Factor of Safety
50 ka

Figure A4.

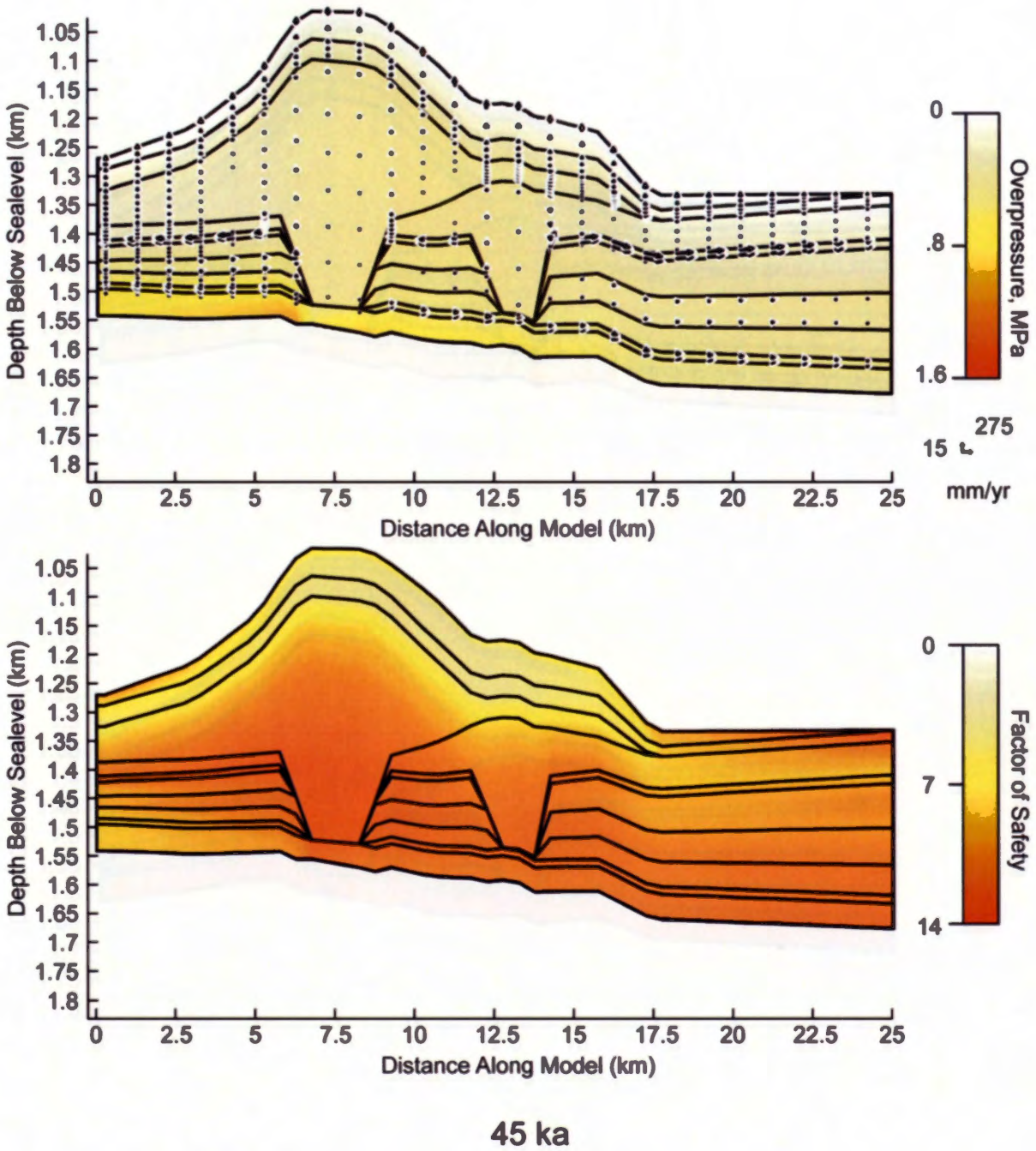
Depth Below Sealevel (km)
1.05
1.1
1.15
1.2
1.25
1.3
1.35
1.4
1.45
1.5
1.55
1.6
1.65
1.7
1.75
1.8
0
2.5
5
7.5
10
12.5
15
17.5
20
22.5
25
Distance Along Model (km)
0
.8
1.6
Overpressure, MPa
275
15
mm/yr
Depth Below Sealevel (km)
Distance Along Model (km)
0
7
14
Factor of Safety
45 ka

Figure A5.

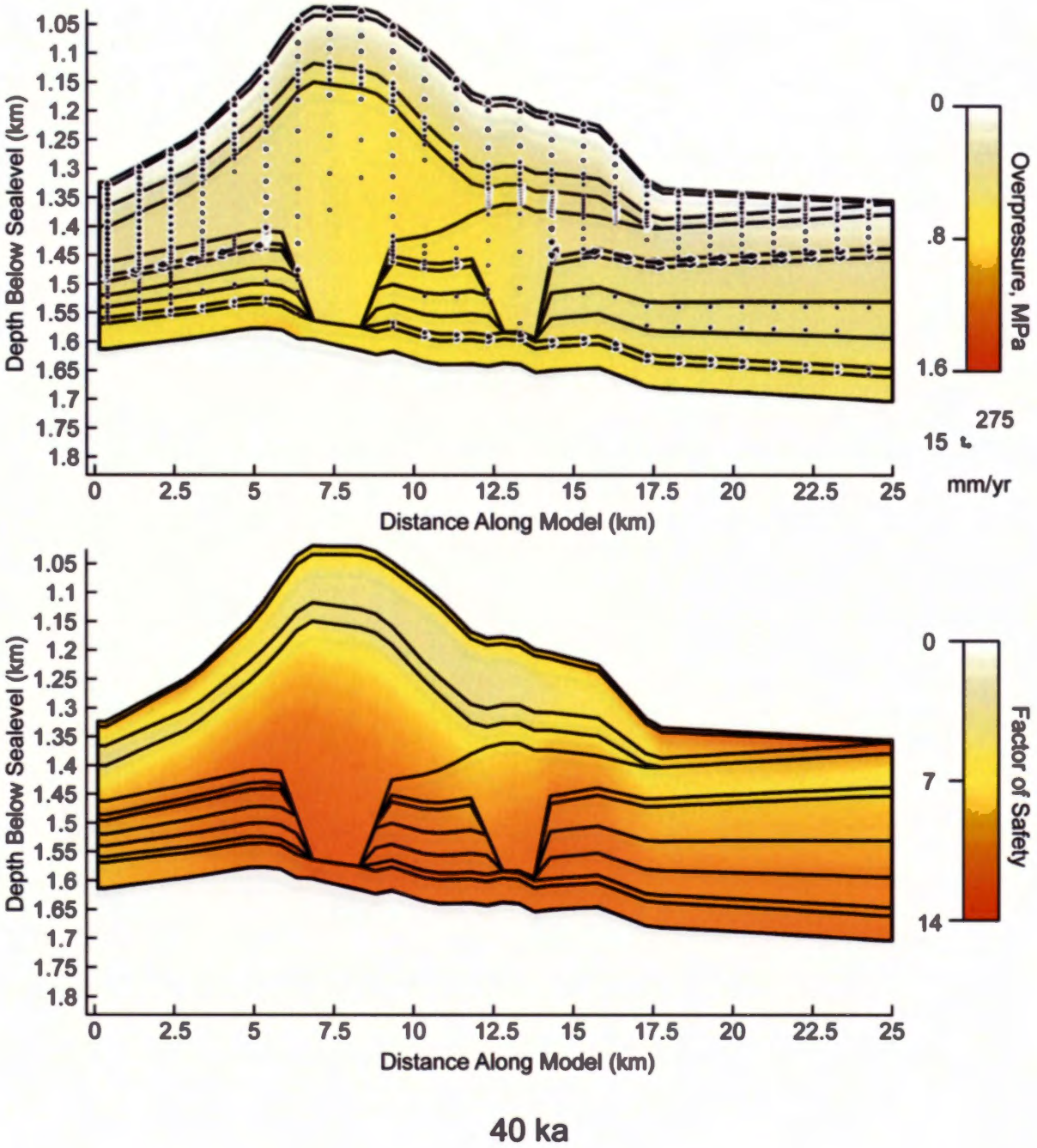
Depth Below Sealevel (km)
1.05
1.1
1.15
1.2
1.25
1.3
1.35
1.4
1.45
1.5
1.55
1.6
1.65
1.7
1.75
1.8
0
2.5
5
7.5
10
12.5
15
17.5
20
22.5
25
Distance Along Model (km)
0
.8
1.6
Overpressure, MPa
275
15
mm/yr
Depth Below Sealevel (km)
Distance Along Model (km)
0
7
14
Factor of Safety
40 ka

Figure A6.

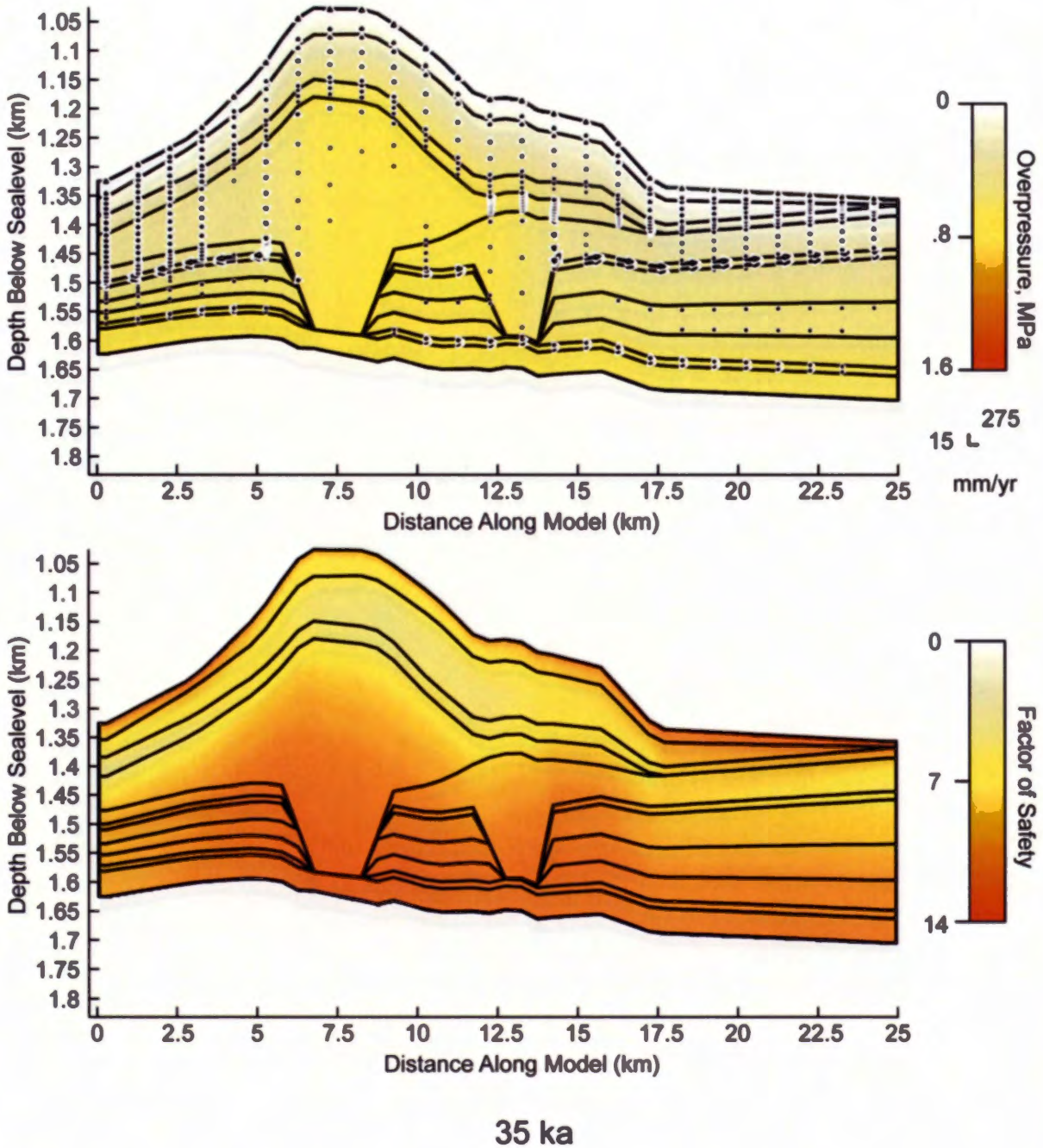
Depth Below Sealevel (km)
1.05
1.1
1.15
1.2
1.25
1.3
1.35
1.4
1.45
1.5
1.55
1.6
1.65
1.7
1.75
1.8
0
2.5
5
7.5
10
12.5
15
17.5
20
22.5
25
Distance Along Model (km)
0
.8
1.6
Overpressure, MPa
275
15
mm/yr
Depth Below Sealevel (km)
Distance Along Model (km)
0
7
14
Factor of Safety
35 ka

Figure A7.

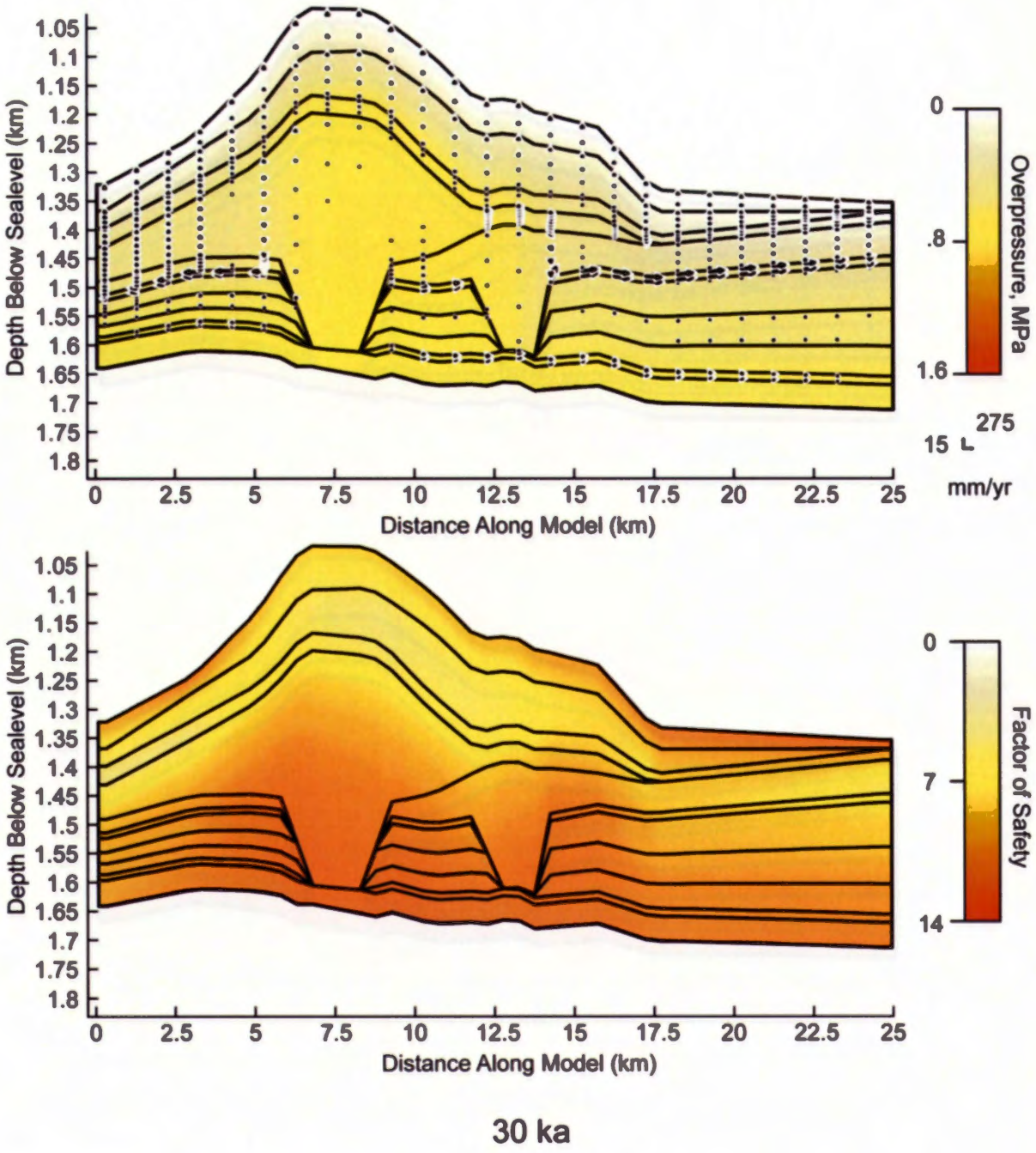
Depth Below Sealevel (km)
1.05
1.1
1.15
1.2
1.25
1.3
1.35
1.4
1.45
1.5
1.55
1.6
1.65
1.7
1.75
1.8
0
2.5
5
7.5
10
12.5
15
17.5
20
22.5
25
Distance Along Model (km)
0
.8
1.6
Overpressure, MPa
15
275
mm/yr
Depth Below Sealevel (km)
Distance Along Model (km)
0
7
14
Factor of Safety
30 ka

Figure A8.

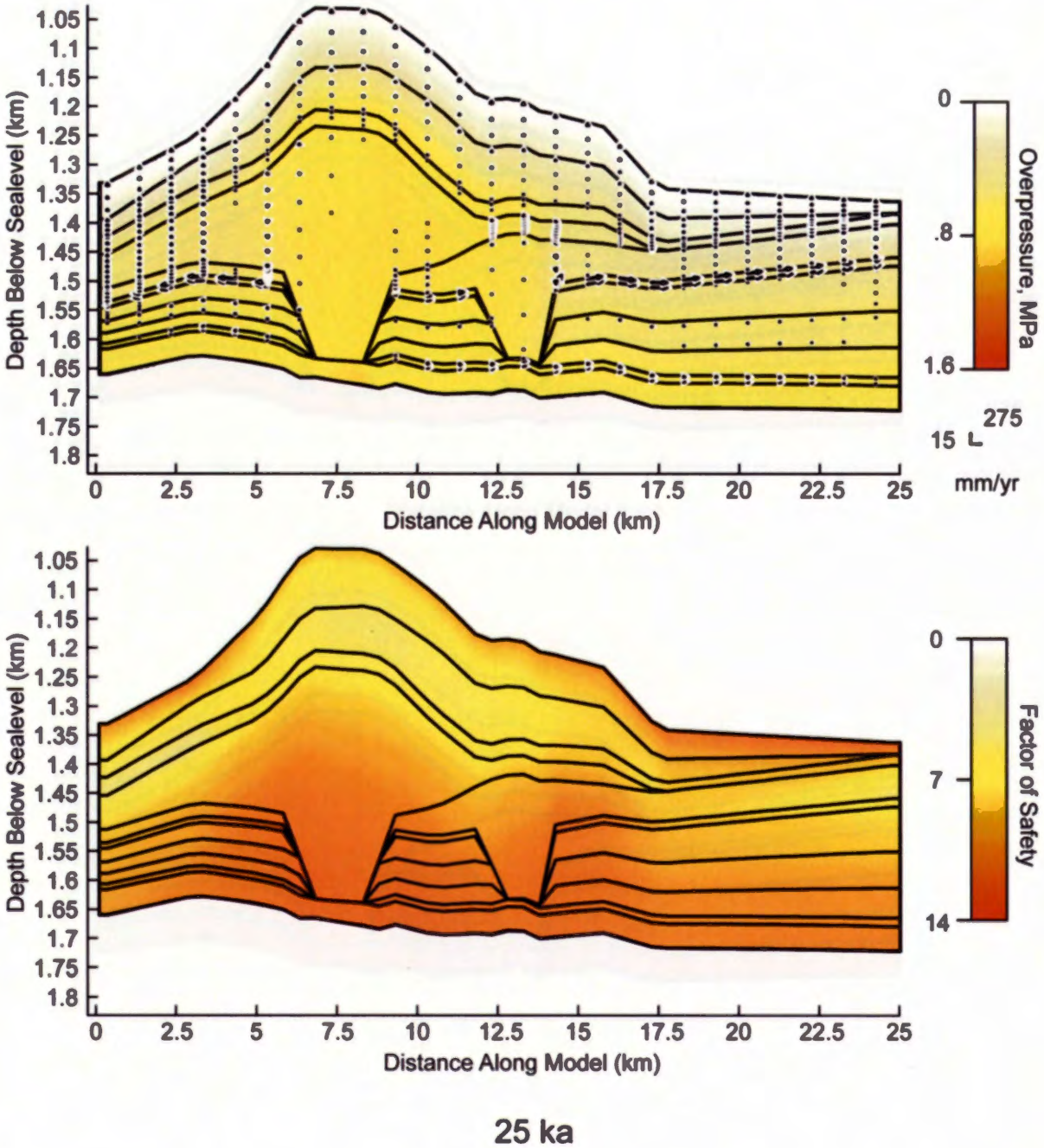
Depth Below Sealevel (km)
1.05
1.1
1.15
1.2
1.25
1.3
1.35
1.4
1.45
1.5
1.55
1.6
1.65
1.7
1.75
1.8
0
2.5
5
7.5
10
12.5
15
17.5
20
22.5
25
Distance Along Model (km)
0
.8
1.6
Overpressure, MPa
15
275
mm/yr
Depth Below Sealevel (km)
Distance Along Model (km)
0
7
14
Factor of Safety
25 ka

Figure A9.

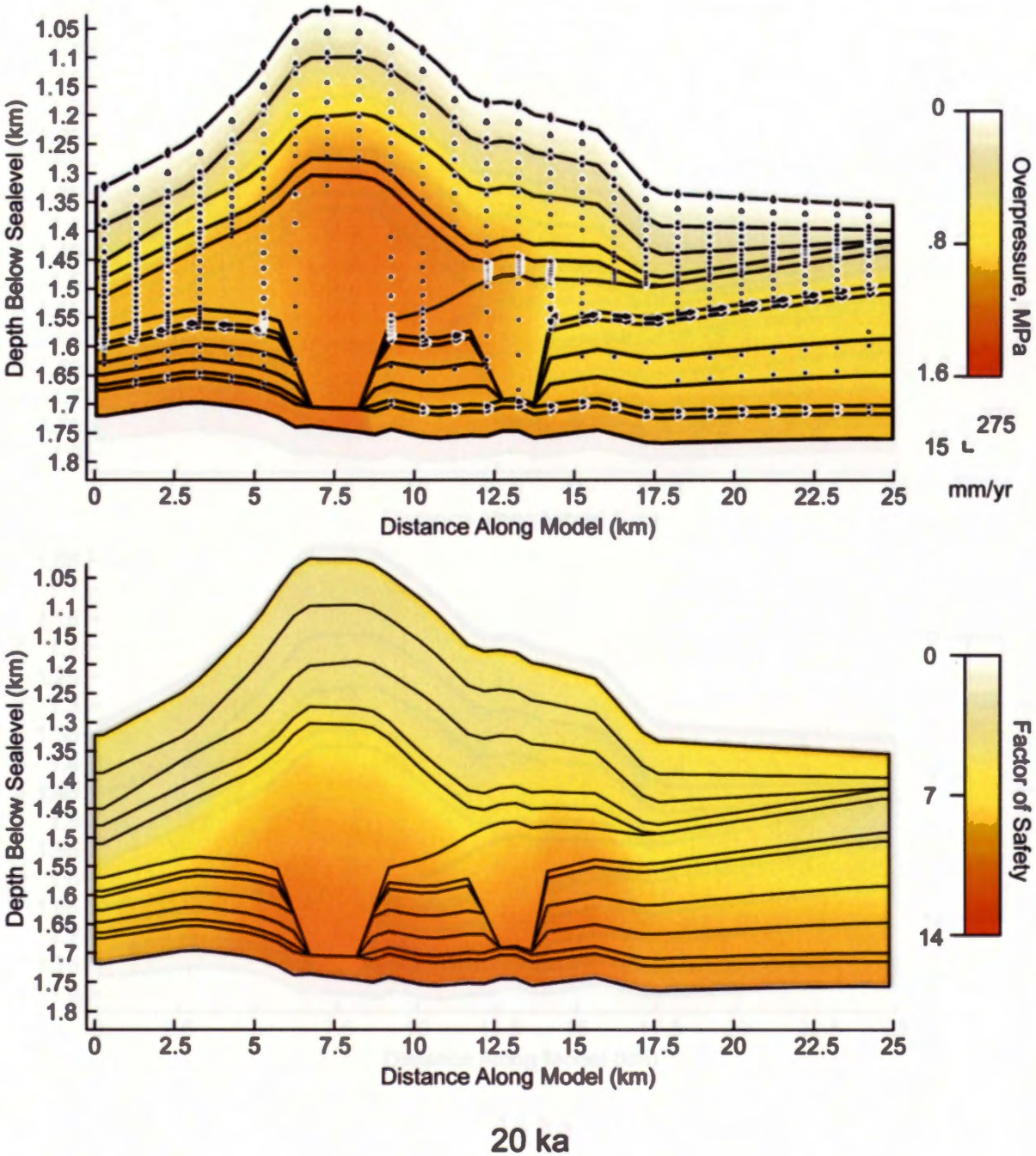
Depth Below Sealevel (km)
1.05
1.1
1.15
1.2
1.25
1.3
1.35
1.4
1.45
1.5
1.55
1.6
1.65
1.7
1.75
1.8
0
2.5
5
7.5
10
12.5
15
17.5
20
22.5
25
Distance Along Model (km)
0
.8
1.6
Overpressure, MPa
275
15
mm/yr
Depth Below Sealevel (km)
Distance Along Model (km)
0
7
14
Factor of Safety
20 ka

Figure A10.

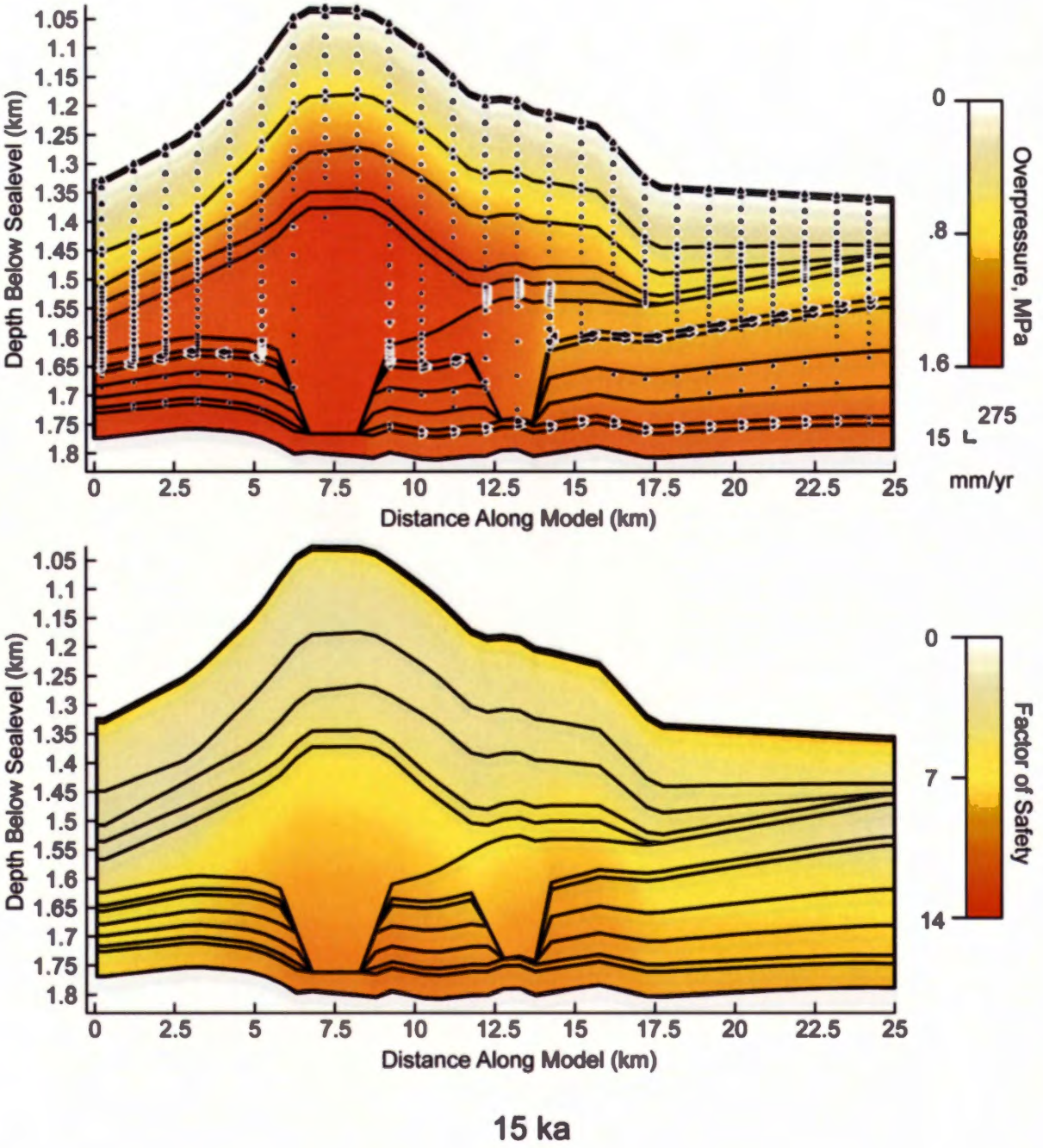
Depth Below Sealevel (km)
1.05
1.1
1.15
1.2
1.25
1.3
1.35
1.4
1.45
1.5
1.55
1.6
1.65
1.7
1.75
1.8
0
2.5
5
7.5
10
12.5
15
17.5
20
22.5
25
Distance Along Model (km)
0
.8
1.6
Overpressure, MPa
15
275
mm/yr
Depth Below Sealevel (km)
Distance Along Model (km)
0
7
14
Factor of Safety
15 ka

Figure A11.

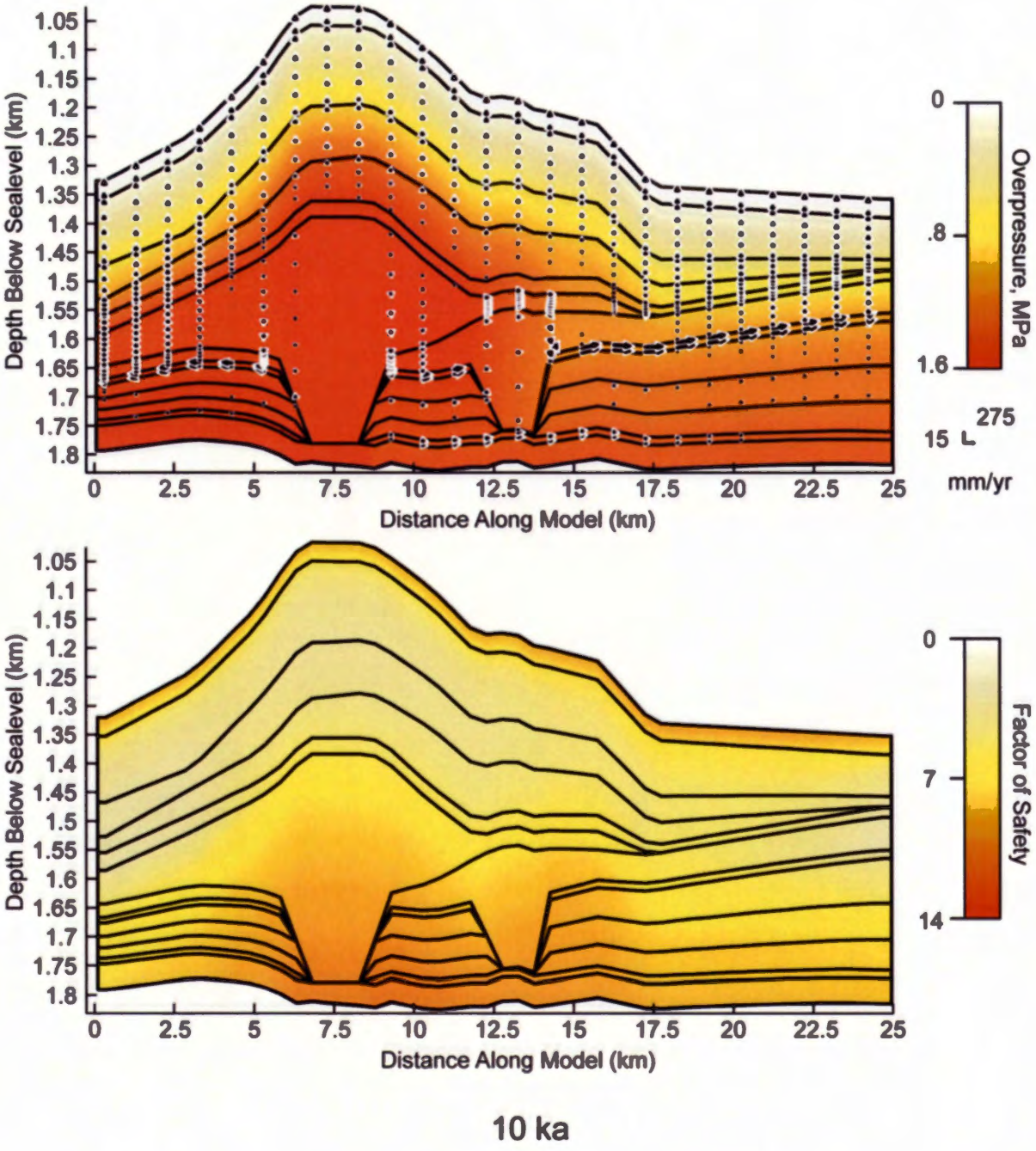
Depth Below Sealevel (km)
1.05
1.1
1.15
1.2
1.25
1.3
1.35
1.4
1.45
1.5
1.55
1.6
1.65
1.7
1.75
1.8
0
2.5
5
7.5
10
12.5
15
17.5
20
22.5
25
Distance Along Model (km)
0
.8
1.6
Overpressure, MPa
15
275
mm/yr
Depth Below Sealevel (km)
Distance Along Model (km)
0
7
14
Factor of Safety
10 ka

Figure A12.

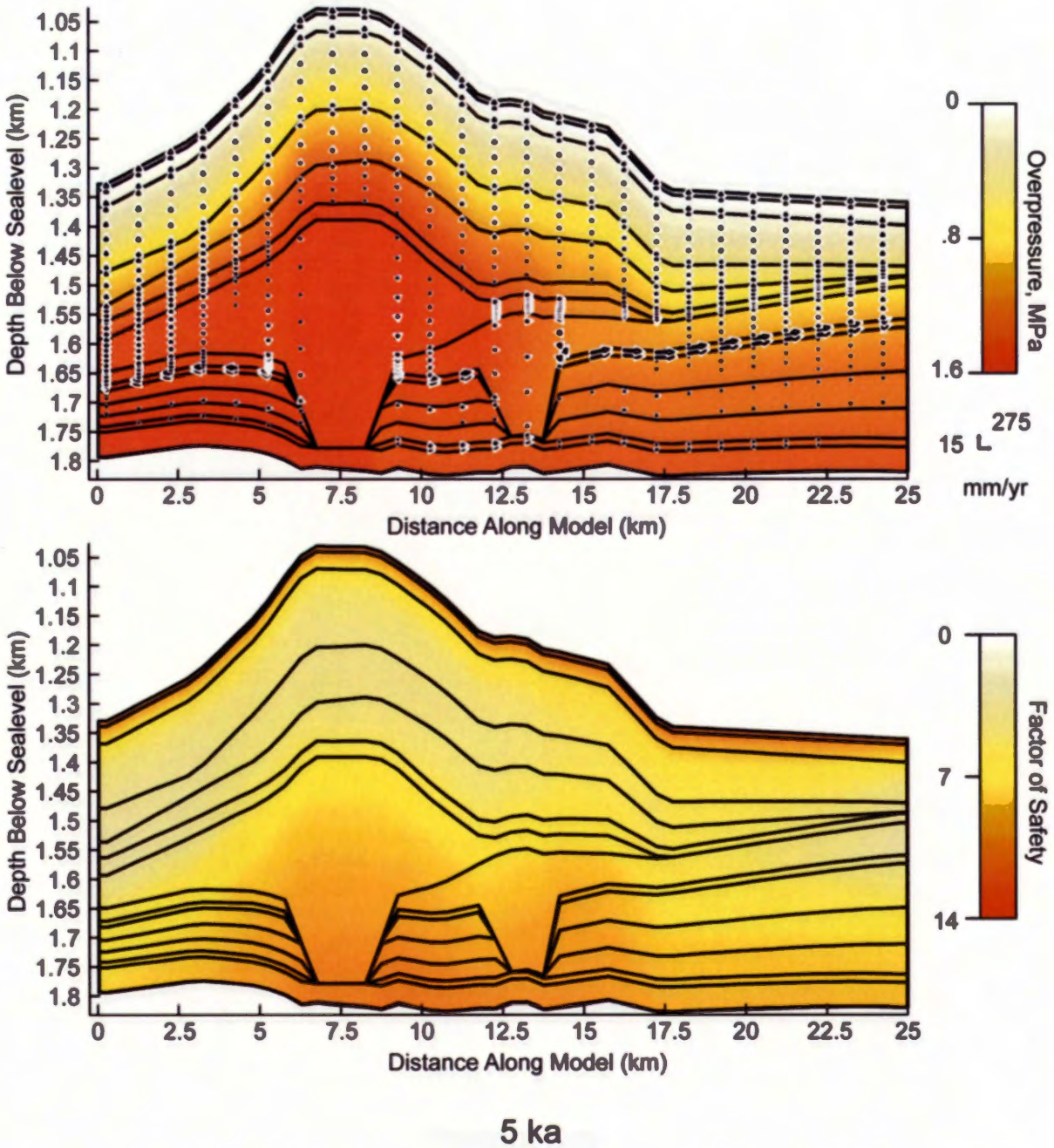
Depth Below Sealevel (km)
1.05
1.1
1.15
1.2
1.25
1.3
1.35
1.4
1.45
1.5
1.55
1.6
1.65
1.7
1.75
1.8
0
2.5
5
7.5
10
12.5
15
17.5
20
22.5
25
Distance Along Model (km)
0
.8
1.6
Overpressure, MPa
15
275
mm/yr
Depth Below Sealevel (km)
Distance Along Model (km)
0
7
14
Factor of Safety
5 ka

Figure A13.

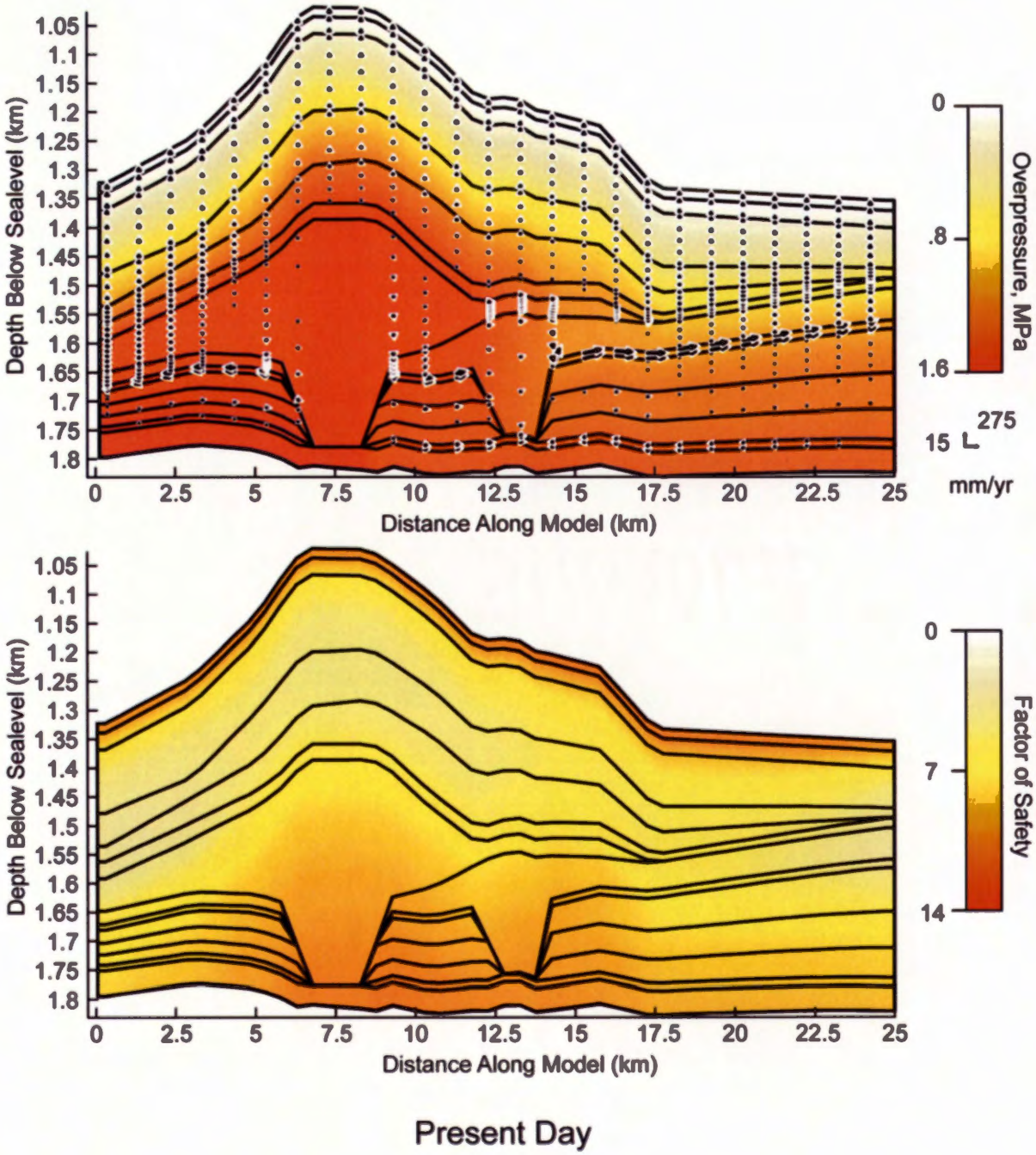
Depth Below Sealevel (km)
1.05
1.1
1.15
1.2
1.25
1.3
1.35
1.4
1.45
1.5
1.55
1.6
1.65
1.7
1.75
1.8
0
2.5
5
7.5
10
12.5
15
17.5
20
22.5
25
Distance Along Model (km)
0
.8
1.6
Overpressure, MPa
15
275
mm/yr
Depth Below Sealevel (km)
Distance Along Model (km)
0
7
14
Factor of Safety
Present Day

Figure A14.